LA-SUB--95-46

HIGH TECHNOLOGY ENGINEERING SERVICES, INC.

FISCAL YEAR 1993 and 1994

RESEARCH AND DEVELOPMENT REPORT

Submitted to the

Los Alamos National Laboratory

In Partial Fullfillment of

Subcontract No. 9-XZ2-7641E

1 October 1994

MASTER

Florence Gamble
President

Michael Gamble
Project Manager

DISCLAIMER

HIGH TECHNOLOGY ENGINEERING SERVICES, INC.

AEROSPACE, NUCLEAR, AND HIGH ENERGY PHYSICS APPLICATIONS
P.O. BOX 28064 PANAMA CITY, FLORIDA 32411 PHONE: (904) 233-8059

FISCAL YEAR 1993 and 1994
RESEARCH AND DEVELOPMENT REPORT

EXECUTIVE SUMMARY

This document has been prepared by the Professional Staff of High Technology Engineering Services, Inc. (HTES) in partial fulfillment of the terms and conditions of subcontract no. 9-XZ2-7641E between HTES and the Los Alamos National Laboratory. During fiscal year (FY) 1993, work was performed for various aspects of mechanical design and analysis, materials development and properties quantification, nuclear environment performance, and engineering program prioritization. The tasks enumerated in the subcontract, attachment B are:

1. Assist in preparation of final R&D report for SDC detector development. From this work a final report shall include but not limited to the findings, recommendations, difficulties, and all financial data including the hours, who worked on the project and the like.

2. Subcontractor shall make contributions to the development of innovative processes for the manufacture of quasi-isotropic, enhanced thermal conductivity compression molded advanced composite materials.

3. Perform finite element analysis as it relates to the Superconducting Super Collider Silicon Tracking System, both mechanical and thermal, of very thin section advanced composite materials.

4. Subcontractor shall perform technical studies, reviews, and assessments of the current program for advanced composites materials processing and testing.

5. Subcontractor shall attend meetings and discussions as directed by MEE-12 technical representative.

According to the subcontract, a deliverable consisting of a report, "detailing all processes developed and the results of all analyses for each task mentioned above shall be submitted no later than September 30, of the government fiscal year."

Unfortunately during the course of FY93, technical and financial challenges prevailed against the aggressive goals set for the program. In point of fact, less than 25% of the contract value was able to be expended due to technical delays and programmatic funding cuts. Also, contracting difficulties with the SSC Lab and financial burdens at Los Alamos totally stopped progress on the subject subcontract during the whole of FY94. This was a great blow to me and the HTES, Inc. technical staff.

Despite the negative influences over the years, significant progress was made in materials properties quantification and development of essential research and development documentation. The following brief report and attendant appendices will address these achievements.

It is my sincere hope that HTES will have the opportunity to provide technical expertise to LANL in the future, under more auspicious circumstances.

Sincerely,

Florence Gamble

Florence Gamble
President

FG:MP

cc: M. Gamble
HTES Chron
J. Sandidge, CPA

HIGH TECHNOLOGY ENGINEERING SERVICES, INC.
FISCAL YEAR 1993
RESEARCH AND DEVELOPMENT REPORT

The overall research and development program of FY93 and FY94 focused on the development of an engineering design for a silicon-based elementary particle tracking system. The attendant engineering analyses, materials sciences studies, prototype fabrications, and progress documentation required to support the design activity were participated in by HTES Technical Staff. The following accomplishments, problems, and general remarks are the opinions of HTES Technical Staff members and in no way reflect an absolute description of the status of the program during FY93 or FY94.

A materials testing program was designed to optimize the engineering materials selection for various components of the silicon tracking system (STS). The ultrastable performance required of that system demands the application of very specialized design materials. The expense of such materials, however, can be exorbitant. For this reason, prudence demands that accurate properties quantification, trade-off studies, and cost / benefit studies be performed to ensure a cost effective design is achieved. An outline for the STS Materials Testing Program can be found in appendix A of this report.

The most impressive specific performance properties for engineering materials are those belonging to advanced composite materials. The advanced composites expected to assume the dominant role in the STS design were carbon fiber-reinforced plastics. This very elite materials class possesses a spectrum of costs and performance, with both generally high. The testing program was designed to identify which fiber and resin combination was most appropriate for cooling ring construction. Epoxy resins were not preferred because of dimensional instability problems. A new, hydrophobic resin system was desired for the application to enhance dimensional stability in the presence of water and liquid butane. The mechanical properties of such resins were not very well defined and required independent testing for confirmation. The results of the mechanical testing program can also be found in Appendices A and B of this report. These results indicate that the mechanical properties of 954-3 cyanate-ester, hydrophobic resin are acceptable for use as an STS cooling ring design material.

Additional testing was sought to verify the dimensional stability of various hydrophobic resins in the presence of water and liquid butane. These tests are difficult to execute accurately. Unfortunately, problems were encountered when the test results from differing institutions varied considerably. Furthermore, the general indication of the test data was that the 954-3 hydrophobic resin was not butane phobic. This was unfortunate because of the time invested in the mechanical test program and the calculations and studies that were continuing assuming 954-3 as the engineering design material of choice. Butane saturation data acquired during this test phase can also be found in Appendix A of this report. A final determination of which resin system is most appropriate for STS cooling design was not possible during FY93 or FY94.

Concurrent with the dimensional stability testing was a thermal conductivity testing program. Enhancement of the thermal conductivity of the STS cooling ring was desired to diminish thermal distortions. Metal fillers were added to the fiber / resin mixture in an effort to increase the cooling ring's transverse thermal conductivity. The length of the constituent fibers was also varied to determine the nature and magnitude of that parameter on transverse thermal conductivity. Once again the data gathered from various test institutions did not correlate well. It was also found that the metal fillers tended to

degrade the mechanical properties of specimens, as did the use of very short fibers, while very long fibers made poor quality speicmens. Finally, it was determined that components composed of resin and longer fibers, approximately 1000 microns or more, without metal additives would be the best choice for STS prototype cooling ring construction. The details of the data analysis and some conclusions of this work can be found in the research publications of Appendices B and C of this report.

A research and development report from ESA-8 to the STS management was required. HTES Technical Staff contributed in the areas of calculation performance and review, mechanical testing, materials sciences, mechanical design, text composition and editing, and overall professionalism. Unfortunately, due to the technical and financial problems during the year, only a rough draft of the document was completed. This rough draft can be found in Appendix C of this report. An additional section of this report containing finite element analyses and materials sciences studies for the outer enclosure and its supports can be found as Appendix D of this report. It has yet to be properly incorporated into the ESA-8 draft document.

Although the accomplishments and contributions of HTES to the LANL FY93 research and development program were nontrivial, accomplishments during FY94 were nonexistent. Generally, the program fell far short of that envisioned at the time of the subcontract's consummation. It is the sincere hope of the HTES Technical Staff that the future will present an opportunity to make up for lost time during the past two years and make a substantial contribution to a LANL program.

APPENDIX A

SDC SILICON TRACKING SYSTEM MATERIALS TESTING PROGRAM

OUTLINE

I. Introduction

A. Motivation for Use of New High Performance Materials

1. Dimensional stability
2. Minimum mass
3. High stiffness

B. Purpose of Materials Testing Program

1. Augment minimal published data
2. Perfect processing techniques
3. Develop confidence in applicability

II. Mechanical Testing

A. Specimen Fabrication

1. Neat resin, longitudinal, transverse, QI
2. Prepreg lay-up, T cure ~177°C, variable plies

B. Test Method

1. Instron & Materials Testing System

2. Elastic properties testing prior to irradiation

i. tensile modules
ii. compressive modules
iii. shear modules
iiii. Poisson ratio

3. Elastic properties testing after irradiation

i. tensile modules
ii. compressive modules
iii. shear modules
iiii. Poisson ratio

4. Inelastic properties testing

i. tensile strength
ii. compressive strength
iii. shear strength

C. Results Evaluation and Comparison to Published Data

D. Results Comparison to Programmatic Requirements

III. Thermal Conductivity Testing

A. Specimen Fabrication

1. Rectangular compression moldings

i. neat resin
ii. resin/fiber
iii. resin/filler
iiii. resin/fiber/filler

2. Arc segment compression moldings

i. resin/fiber
ii. resin/fiber/filler

B. Test Method

1. Flash diffusivity
2. Direct Contact

C. Results Evaluation and Comparison to Published Data

D. Results Comparison to Programmatic Requirements

IV. Coefficient of Thermal Expansion Testing

A. Specimen Fabrication

1. Neat resin, longitudinal, transverse, QI
2. Prepreg lay-up, Tcure ~177°C, 8 plies

B. Test Method

1. Optical comparitor
2. Laser Interferometer
3. T_{test} ~30°C

C. Results Evaluation and Comparison to Published Data

D. Results Comparison to Programmatic Requirements

V. Coefficient of Moisture Expansion Testing

A. Specimen Fabrication

1. Neat resin, longitudinal, transverse, QI
2. Prepreg lay-up, Tcure ~177°C, XX plies

B. Test Method

1. Optical Comparitor
2. $-83°C \leq T_{test} \leq 200°C$

3. XX≤ RH_{test} ≤XX
4. O≤ t_{test} ≤ 400 hours
5. Witness coupon weight measurement

C. Results Evaluation and Comparison to Published Data

D. Results Comparison to Programmatic Requirements

VI. Conclusions

A. Overall Materials Selection Standing

1. Performance commensurate w/Programmatic Requirements
2. Cost versus Performance

B. Additional Testing

1. Reaffirm ambiguous results
2. New investigative thrusts
3. Pray for enlightenment!

Properties of P75/954-3 Laminate Samples (60% Vf)

	Property	Data Source	Coupon Description				Comments
			Neat	0°	90°	QI	
1	Elastic Tensile Mod	LANL	0.54	46.80	1.00	14.40	
	(Msi)	LANL*	0.51	46.60	0.96	15.90	*
		Fiberite	-	43.80	-	-	
		Ketema	0.55	47.00	0.93	14.00	
		Sandia NL	0.53	40.44	1.18	14.14	
2	Elastic Comp Mod	LANL	-	43.60	0.97	11.80	
	(Msi)	LANL*	-	41.10	0.99	11.80	*
		Fiberite		35.50			
		Ketema	0.50	39.00	0.90	11.20	
		Sandia NL					
3	Elastic Shear Mod	LANL	0.18	0.65	0.24	-	
	(Msi)	LANL*	0.18	0.69	0.25	-	*
		Fiberite					
		Ketema	0.17	0.58	0.23	-	
		Sandia NL	0.20	0.64	0.38	-	
4	Poisson's Ratio	LANL	0.38	0.25	0.0043	0.28	
		LANL*	0.37	0.25	0.0031	0.31	*
		Fiberite	-	-	-	-	
		Ketema	0.40	0.32	0.0063	0.33	
		Sandia NL	0.40	0.32	0.0060	0.33	
5	Ult Tensile Strength	LANL	-	-	-	-	
	(Ksi)	LANL*	-	-	-	-	
		Fiberite	-	-	-	-	
		Ketema	8.54	145.40	3.40	42.60	
		Sandia NL	-	-	-	-	
6	Ult Comp Strength	LANL	-	-	-	-	
	(Ksi)	LANL*	-	-	-	-	
		Fiberite	-	-	-	-	
		Ketema	-	48.90	6.05	19.00	
		Sandia NL					
7	Ult Shear Strength	LANL	-	-	-	-	
	(Ksi)	LANL*	-	-	-	-	
		Fiberite	-	-	-	-	
		Ketema	3.93	5.68	2.82	-	
		Sandia NL					
8	CTE	COI	27.62	-0.70	14.42	-0.13	
	(ppm/°C)	Fiberite	-	-0.80	-	-	
9	CME Strain	COI	238.00	3.00	229.00	11.30	Weight data required
	(ppm)						

* indicates environmentally conditioned coupons

Butane Saturation Test

	Coupon	1	2	3	4
	Material	TEM 9000	RS-3	954-3	P75/954-3
		Neat Resin	Neat Resin	Neat Resin	Compression molded
	Description	coupon w/ hole and notch	rectangular coupon	coupon w/ hole and notch	arc segment
	Color	translucent amber	opaque brown	opaque brown	black
3/22/93	Initial Weight grams	2.6526	4.1332	2.6228	1.693
3/23/93	Bakeout Weight grams	2.6467	4.126	2.6053	1.6911
	Hours to Bakeout	24	24	24	24
3/24/93	10:26AM begin immersion	2.6467	4.126	2.6053	1.6911
3/24/93	5:00PM	2.6456	4.1333	2.6086	1.6927
3/25/93	5:00PM	2.6461	4.1522	2.6333	1.6921
			*	*	
3/26/93					
3/29/93					
3/30/93					
3/25/93	% wt gain	-0.02%	0.63%	1.07%	0.06%
*Note considerable shape change on these parts (curling)					

APPENDIX B

SILICON-BASED ELEMENTARY PARTICLE TRACKING SYSTEM: MATERIALS SCIENCE AND MECHANICAL ENGINEERING DESIGN

W. O. Miller, M. T. Gamble, T. C. Thompson, and J. A. Hanlon
Los Alamos National Laboratory
Los Alamos, New Mexico 87545

ABSTRACT

Research and development of the mechanical, cooling, and structural design aspects of a silicon detector-based elementary particle tracking system has been performed. Achieving stringent system precision, stability, and mass requirements necessitated the use of graphite fiber-reinforced cyanate-ester resins. Mechanical test results of the effects of butane, ionizing radiation, and a combination of both on the mechanical properties of these materials are presented, as well as progress on developing compression molding of an ultralightweight graphite composite ring structure and TV holography-based noninvasive evaluation.

Keywords: particle tracking system, mechanical design, composite materials, dimensional stability, thermal conductivity, compression molding, TV holography.

1. INTRODUCTION

Los Alamos National Laboratory is researching and developing a silicon detector-based elementary particle tracking system for use in the world's largest high-energy physics experiment to be located in the United States.[1] This silicon microstrip detector-based system, termed silicon tracking system (STS), is composed of detectors arranged in both a cylindrical array and an array of flat panels about the interaction region. The overall length of the STS is 5.16 m, while the maximum diameter is 0.93 m. For the STS to achieve its physics goals, its mechanical structures and services must

- support 17 m^2 of silicon microstrip detectors and stabilize their positions to within 5 μm,
- uniformly cool the detector system to 0°C, while potentially removing up to 13 kW of waste heat generated by the detector electronics,
- provide up to 3400 A of current to supply 6.5 million electronics channels,
- supply all control and data transmission lines for those channels,
- minimize mechanical structure and use low-Z materials, and
- remain dimensionally stable throughout exposure to 10 Mrad over a 10-year period.

The method for supporting the individual central region silicon layers combines adjacent layers into a silicon shell, as shown in Figure 1. Central region silicon shells are supported pairwise by two composite support cylinders composed of graphite/cyanate-ester resin (G/C-E) to minimize structural materials while maximizing stiffness and dimensional stability. The maximum silicon detector module length in the central region is 24 cm. Each silicon module is stiffened by edge-bonding two 0.125-mm-thick G/C-E strips along the length of the detector edges. These silicon modules are then bonded to the structural rings made from G/C-E to form the silicon shell assembly. Besides providing structural support, these rings, hereafter denoted cooling rings, contain an internal heat pipe wick artery structure. Because the detectors in the central region are canted at an

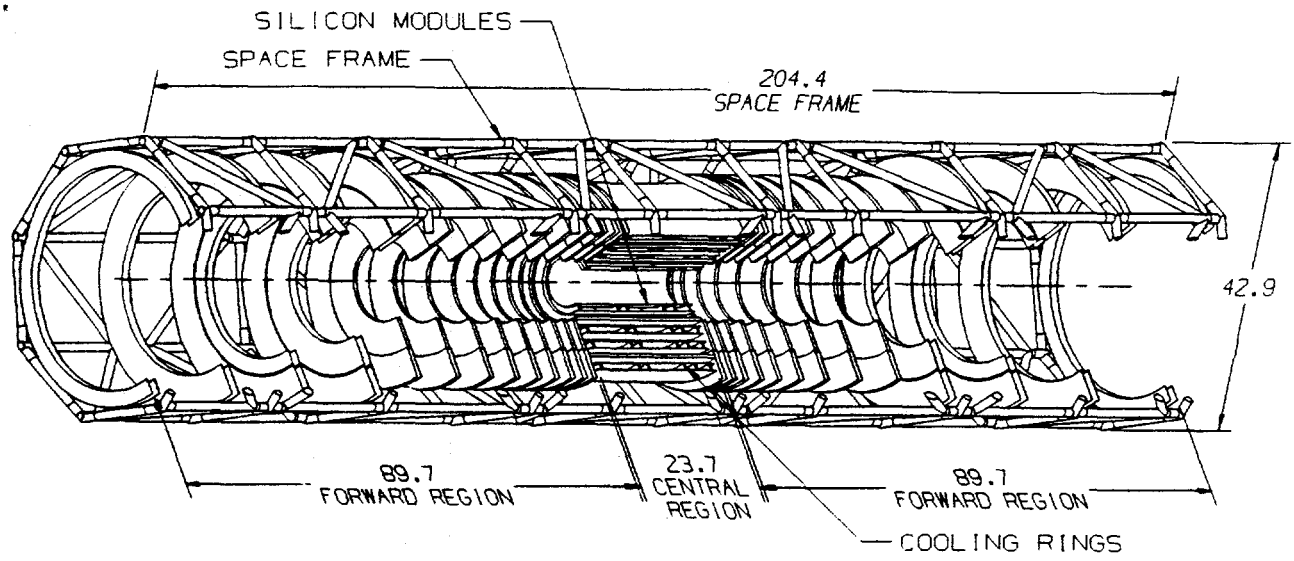

Figure 1. Silicon arrays with space frame (cutaway view).

angle of 7.4°, the top and bottom surfaces of the cooling ring assume a serrate geometry. Electronics mounted at each end of the module assemblies generate heat, which flows through the thin-walled composite cooling ring surface facets onto which the module is mounted and evaporates the cooling fluid.

A dimensionally stable metal matrix composite (MMC) space frame will provide structural support for the central and forward regions. Ultrahigh elastic modulus, immunity to moisture-induced distortions, and tailorability of coefficient of thermal expansion (CTE) motivated this selection. Aluminum and magnesium matrices, combined with P-120 fibers at 60 v/o are candidates that yield axial moduli of 525 GPa and 515 GPa with CTEs of –0.25 ppm/°C and –0.6 ppm/°C, respectively.

An ultralightweight G/C-E sandwich construction enclosure contains evaporated butane vapor and provides for the transfer of STS mechanical support loads. This shell and its end cover plates have an areal density of only 1.2 kg/m^2. Experimental quasi-isotropic (QI) panels of 250-μm-thick P-75 graphite and1939-3 epoxy were irradiated, using protons, at a fluence of 10^{15} particles/cm^2, representing 10 operational years. Out-of-plane mechanical distortions were measured to be less than 5 μm, instilling confidence in the general material selections and the construction approach. A 0.5-mm beryllium inner liner will complete this stiff, low-mass structure.

2. MATERIALS CONSIDERATIONS AND TESTING

Stringent detector precision required materials capable of maintaining dimensional stability in the presence of thermal gradients, moisture, ionizing radiation, and volumetric deviations caused by butane vapor ingress. The requirement to minimize system structural mass while providing a stiff support for the silicon detection media further complicates the design. Beryllium is nearly transparent to particles and impervious to moisture and butane. Unfortunately, it has a large CTE, is very costly, and requires complicated machining procedures. G/C-E materials are a good compromise, having more favorable particle interaction characteristics than monolithic metals and more favorable CTE, cost, and fabrication characteristics than beryllium. The STS' environmental factors required special consideration because the performance of G/C-E exposed to a combination of butane and ionizing radiation is not well known. For this reason, a testing program, was undertaken, in which mechanical properties were verified before and after environmentally conditioning the coupons in a butane filled container, and irradiating them with a cobalt gamma ray source. These results are shown in Table 1.

LANL and one independent testing organization used similar, conventional (CONV) load frame- and load cell-based tests. A third organization used nondestructive evaluation (NDE) methods–scanning electron micros-

Table 1. Mechanical properties test results for P-75S/954-3 laminates normalized to 60% fiber volume fraction.

Mechanical Property	Test Institution	Specimen Description			
		Neat	0°	90°	QI
Elastic Tensile Modulus (GPa)	LANL	3.7	323	6.9	100
	LANL*	3.4	321	6.6	110
	CONV	3.8	324	6.4	96.5
	NDE	3.7	280	8.1	97.5
Elastic Comp. Modulus (GPa)	LANL	3.7	300	6.7	81.3
	LANL*	3.5	283	6.8	81.3
	CONV	3.4	270	6.2	77.2
Elastic Shear Modulus (GPa)	LANL	1.2	4.5	1.7	—
	LANL*	1.1	4.8	1.7	—
	CONV	1.2	4.0	1.6	—
Poisson's Ratio	LANL	0.38	0.25	0.0043	0.28
	LANL*	0.37	0.25	0.0031	0.31
	CONV	0.40	0.32	0.0063	0.33
	NDE	0.40	0.32	0.0060	0.33
Ultimate Tensile Strength (MPa)	CONV	60	1000	23.4	294
Ultimate Comp. Strength (MPa)	CONV	—	337	41.7	131

*Denotes results for specimens environmentally conditioned by 10 Mrad and butane.

copy and scanning acoustic microscopy–to determine the elastic properties of specimens.[2] The data generated by all institutions and methods were comparable, and closely matched published data including manufacturer's specifications. The overall conclusion of the mechanical properties test program is that the P-75/954-3 materials system is now mechanically fully qualified and is acceptable for achieving STS baseline performance objectives.

The coefficient of moisture expansion (CME) for hydrophobic resins has been well documented.[3] The STS application, however, will require dimensional stability in the presence of butane vapor at 0°C. Investigations of the strain, saturation level, and time constant for this phenomenon are promising. The quality of the laminate will have an effect on its uptake and as its mechanical performance. Quality has been investigated using ultrasonic techniques, such as pulse-echo scanning and time-of-flight measurements. These techniques were used to quantify the NDE elastic mechanical properties of Table 1 and to evaluate the quality of thin, compression-molded cooling rings.[4] Figure 2 demonstrates an example of pulse-echo scanning applied to a segment of a cooling ring.

3. COOLING RING DEVELOPMENT

The need for dense, high-fiber-volume, high-quality, QI cooling rings motivated the use of compression molding for their fabrication. An incremental approach was required, because of manufacturing challenges, and because of the need to fabricate a 360° cooling ring with a 400-μm-thick wall of serrated geometry using P-75/C-E molding compound.[4] The frailty of these thin-walled components, composed of very brittle P-75 fiber-based molding compound, necessitated using a 30° arc segment mold and commercially available molding compounds such as those available from ICI Fiberite, Inc., for initial attempts. Arc segments were

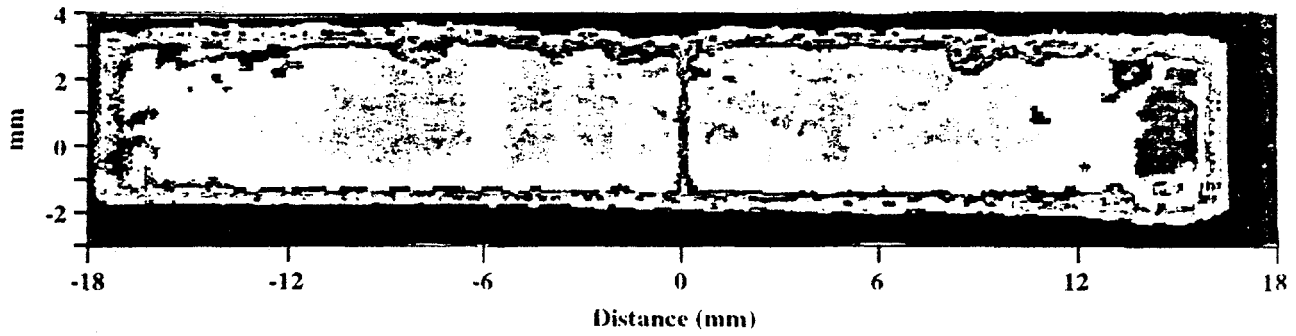

Figure 2. Image of pulse-echo amplitude variations indicating where compositional changes occur within the composite (top view).

fabricated from a mold that produced components with 450-μm-thick walls using 6-mm-long fibers in the phenolic base with 58 v/o fiber and 32 v/o resin. The fiber length was reduced from 12 mm because of flow problems encountered.

An improved 120° arc segment mold was fabricated to produce 400-μm-wall-thickness ring arcs composed of intermediate-modulus graphite fibers, approximately 90 μm long, in a toughened epoxy resin. High viscosity hindered the success of all arc segments bearing more than 45 v/o fibers. High viscosity also hindered the fabrication of high-P-75-fiber volume 120° arc segments in which TEM 9000 resin was used.

The hydrophobic C-E resin to be used in the STS cooling rings is ICI Fiberite, Inc.'s 954-3. This resin's viscosity is nearly 100 times lower than that of TEM 9000 epoxy; hence, a materials system using 954-3 flows well at 45 v/o of fiber. Problems in releasing arc segments from the mold were overcome by selecting the proper mold coating and mold release agents. A post-curing mandrel mitigated ejection breakage.[4]

Satisfactory progress was made toward the intermediate objective of producing dense, 60% fiber volume, high-quality, 120° arc segments composed of P-75/C-E based molding compound. A photograph of a successful cooling ring arc segment, produced with P-75/C-E molding compound of 45 v/o fiber, is shown in Figure 3. The single remaining obstacle for this stage is the successful use of P-75 fibers longer than 90 μm, potentially up to 1600 μm, for the production of 400-μm-wall-thickness components with higher fiber volume fraction.

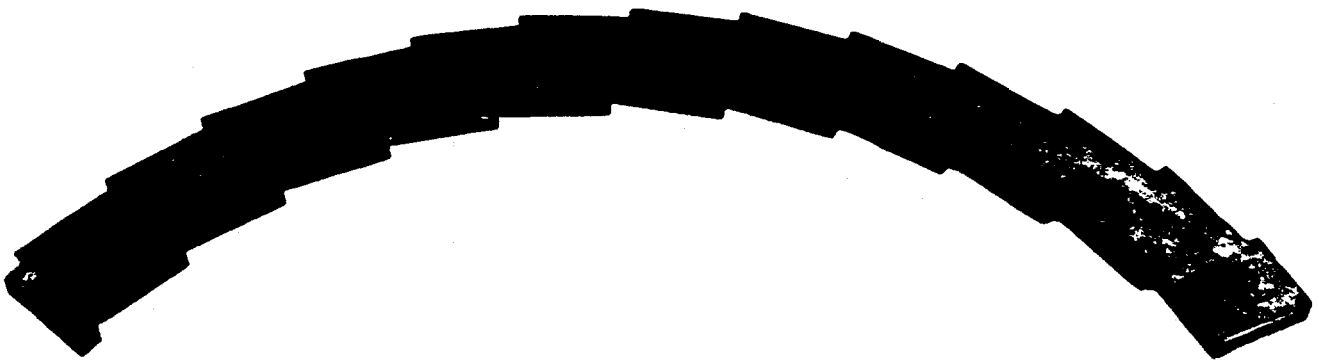

Figure 3: Photograph of a cooling ring arc segment bearing 45 v/o P-75 fibers and 55 v/o epoxy resin (cross-sectional view).

4. MATERIALS BULK PROPERTIES ENHANCEMENT

Exacting precision-tracking design goals required maximizing key composite materials bulk properties used for supporting the delicate silicon modules. Compression molded cooling rings mechanically support the silicon detectors and provide a thermally conductive path for removing heat dissipated from the electronic modules. The latter requires minimizing the thermal gradient transverse to the cooling ring wall. Consequently, the elastic modulus and thermal conductivity properties achievable with compression molding were a primary concern. An experimental program was undertaken to enhance the transverse thermal conductivity (k_t) of the C-E resin-based compression moldings. Test samples were produced using aluminum nitride (AlN) particles, diamond particles, and discontinuous, randomly oriented graphite fibers both separately and in particle/fiber combinations. The thermal conductivities of these substances are 0.2 W/m°C, 180 W/m°C, 18 W/m°C, 280 W/m°C, and 2000 W/m°C for the C-E resin, P-75 fiber longitudinal, P-75 fiber transverse, AlN, and diamond particles, respectively. Specimens were cut from 3.2-mm compression-molded disks and their thermal conductivities were determined using laser flash diffusivity. A maximum additive volume fraction of 27% was tested and compared with published data for resin thermal conductivity enhancement.[4] These data suggested that a significant increase in conductivity would not be realized at such low additive volume fractions.

Test samples were produced using P-75 fibers compression molded with C-E resin for comparison with the particulate additive samples. The fiber lengths varied from 90 to 600 μm with an average length of approximately 100 μm. Fiber volume fractions of 45% to 56% were tested. Ultimately enhancement of the neat resin's thermal conductivity, while reinforcing it with the P-75 fiber, was sought. The objective was to use short fibers, approximately 100 μm long, whose aspect ratio (AR) was more than 10, to demonstrate "long-fiber" reinforcement characteristics per theoretical predictions. Specific processing steps were taken to effect random fiber orientation as a means to achieve a QI, low-CTE composite with an enhanced thermal conductivity. It was anticipated that this would considerably enhance the cooling ring k_t because the 400 μm-wall-thickness could be spanned by a few fibers, effectively producing a psuedo percolation effect nominally accomplished by an agglomeration of 5- to 25-μm effective-diameter particles. Alternatively, enhancement by single fibers spanning the thickness would result in taking maximum advantage of the 180 W/m°C longitudinal thermal conductivity of P-75 fibers. The ultimate goal of adding a high thermal conductivity metal to the P-75/C-E system to produce a high modulus, high k_t cooling ring continued to seem feasible until several cooling ring arc segments were produced with AlN, 11 v/o, and P-75 fiber, 39 v/o. The k_t of these partial rings was enhanced, as expected, but those with a solids content above 50 v/o were very brittle and, hence, indicated the infeasibility of this approach.

The design parameters of the STS could be achieved using a cooling ring with a k_t of 4 W/m°C. This was now to be accomplished using only the P-75/C-E combination. Subsequent mechanical tests on the specimens bearing 100-μm-long fibers revealed very low mechanical properties, in the range of those expected from short-fiber reinforcement. This result warranted additional investigation. In the interim, 400-μm-long P-75 fibers were used in cooling ring arc segment samples to promote improved moldability of extremely thin sections and to achieve more single fibers spanning the wall thickness for enhanced k_t. Figure 4 illustrates the measured k_t for cooling rings with a 60/40 volume fraction ratio for fiber/resin content. Thermal conductivities very near the design goal were obtained. The k_t data for composite ring specimens produced with 100-μm-long fibers were decidedly lower. Thermal conductivity data obtained from a carbon/phenolic molded ring with relatively long fibers is included for further comparison. Chamis[5] and Springer[6] present theoretical models for k_t characteristic of continuous graphite fiber/polymeric resin systems. These models were used as a baseline for assessing k_t enhancement of the discontinuous fiber system.[4] Figure 4 demonstrates that the enhancement factor approaches seven.

Sheng's prediction[7] for a randomly oriented, acicular ("needle-like") particle with an AR of 10 is depicted in Figure 4. This AR is similar to that of the 100-μm-long fibers. Similar predictions exist for the major axis of ellipsoidal particles oriented normal to the direction of heat flow.[5] For this case, the predicted thermal

conductivity is similar in magnitude to Chamis model at fiber volume fractions less than 40%. For both higher fiber volume fractions and randomly oriented fibers, Sheng's model predicts considerable thermal conductivity enhancement.

The Lewis-Nielsen model[8] can be used to characterize the elastic modulus as a function of fiber AR and volume fraction, as was done for k_t enhancement, because both are bulk material properties, as previously indicated. Using this model, it is possible to predict the elastic tensile modulus to resin modulus ratio for the composite as a function of fiber AR and volume fraction for longitudinal fiber orientation. At a fiber AR of 1000, the modulus ratio for 60% fiber volume fraction is 82.11, which approaches a continuous unidirectional fiber matrix. For AR = 10000, the modulus ratio is 83.6. For the C-E resin, a tensile modulus of 3.7 GPa was established. Hence, the predicted composite modulus for the long fiber of 0.1 m would be 309.3 GPa per Nielsen. This agrees with the test value of 321.3 GPa to approximately 4%. This exercise demonstrated that fiber reinforcement AR must be greater than 100 to approach the stiffness of a continuous fiber composite. This represents a factor of 10 greater length for total shear stress transfer than yielded by theoretical predictions. Longer fiber reinforcement has a negative influence on cooling ring fabricability as previously stated, but is overridden by mechanical performance concerns.

Attainment of high cooling ring stiffness, indicating a large composite elastic modulus, E_c, mandates a high fiber volume fraction. For an AR of 100, a 60% fiber volume fraction produces a factor of 1.7 greater stiffness over 40%. The improvement in stiffness is also apparent at lower fiber ARs. Most cooling ring specimens were fabricated using fiber ARs on the order of 10 to 40, with random orientation. The bulk properties of such a complex matrix, however, can be predicted. Figure 5 demonstrates two- and three-dimensional predictions and test data for published models.[4] These data are plotted at a nominal AR of 10, corresponding to a fiber length of 100 µm. Acid digestion tests indicate that the fiber volume fraction was approximately 45%, considerably below the goal of 60%. It is difficult to estimate the extent to which the composite approaches a highly three-dimensional matrix. A review of arc-segment photomicrographs suggests that for compression-molded components, the composite is three-dimensional, but not homogenous. At an AR of 1000, the elastic modulus has a definite positive slope. Extrapolating the modulus calculation to an AR equal to 10000 results in a value of 118 GPa for the two dimensional case. This value is close to the 98 GPa measured on QI continuous fiber coupons. These results indicate that the Nielsen model for elastic modulus can provide a reasonable approximation for composite bulk properties over a range of discontinuous to continuous fiber reinforcement.

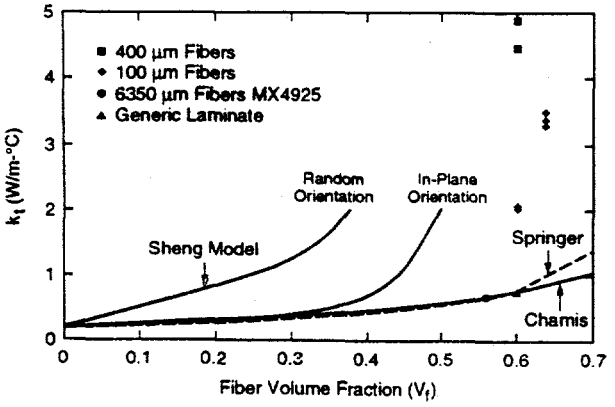

Figure 4. K_t of 450-µm-thick cooling ring segments from compression-molded P-75/C-E discontinuous fibers (100µm, 400µm).

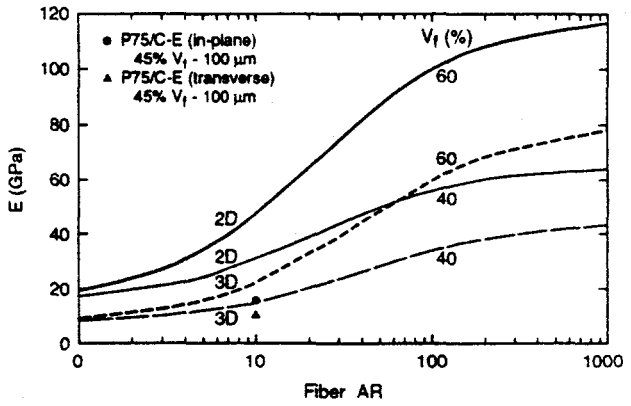

Figure 5. E_c versus fiber AR, for two- and three-dimensional randomly oriented fibers at 60% and 40% V_f.

5. TV HOLOGRAPHIC NONINVASIVE EVALUATION

Long-term dimensional stability and dynamic behavior of the STS will be evaluated absolutely noninvasively with submicron accuracy using TV, or electro-optic, holography. Similar to classical interferometry, in which an object beam and a reference beam interact forming fringe patterns, TV holography will be used to produce holographic fringes containing information about STS shape changes. These fringes will be gathered by a TV camera, instead of on film, input into a computer, and computationally interfered with a baseline state of the STS to determine the magnitude of environmentally induced static or dynamic deformations. This extension of classical holography allows three dimensional, diffusely reflecting, nonplanar surface motions to be quantified in near real-time. Figure 7 demonstrates a static thermal stress gradient whose source was the heat from a human hand placed near a silicon detector module, deforming the 24-cm-long assembly by approximately 0.6 μm. The dynamic capability of TV holography is demonstrated by Figure 8 in which fringes describing the fundamental natural vibration frequencies of bending and torsion of a silicon module are shown. The fundamental bending mode of 94.16 Hz and the torsional mode of 113 Hz were acoustically excited and recorded. The characteristic contours of the fringe patterns express the mode shape. The magnitudes of the vibratory displacements can be determined from the fringe density.

6. CONCLUSIONS

Several conclusions are clear from the STS' materials science and mechanical design information presented herein. The use of C-E-based composite materials for applications requiring dimensional stability in the presence of a combination of ionizing radiation and butane is feasible. Elastic and inelastic mechanical properties were found to be affected negligibly by 10 Mrads of dose in a butane-filled cannister. Absorption and strain measurements are underway to quantify the butane saturation level and coefficient of butane absorption for the 954-3 and other C-E resin systems.

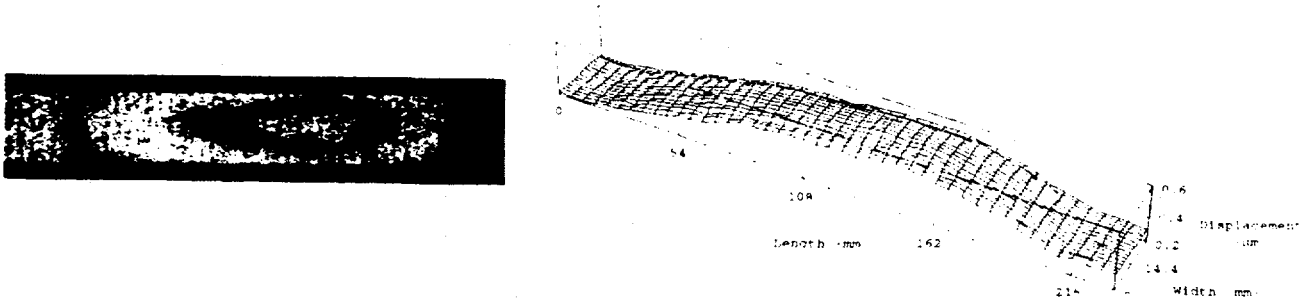

Figure 6. TV holography fringe pattern (left) and computer reconstruction (right) of a silicon module's thermally-induced static deformation of 0.6 μm.

Figure 7. TV holography fringe patterns of a silicon module's fundamental dynamic bending mode of 94.16 Hz (left) and torquing mode of 113 Hz (right).

Success with compression molding 400-μm-wall-thickness cooling ring arc segments composed of 60 v/o, 90-μm-long, P-75 fibers and 40 v/o, 954-3 C-E resin is encouraging. Maximum cooling ring mechanical and thermal properties will be attained using molding compounds bearing high-fiber volume fractions of long fibers, whose ARs are near 100 and whose lengths are approximately 1000 μm. This fact was gleaned from published data and from extensive resin k_t enhancement attempts using monolithic metal additives in conjunction with high-modulus graphite fibers. Charge deposition and cure cycle optimization must be accomplished to enable production of dense, high-quality components using long P-75 fibers.

Static and dynamic TV holography tests of silicon modules experiencing bending and torsion were very successful. The capability to quantify STS shape changes to the submicron level will provide useful information regarding the system's long-term dimensional stability.

REFERENCES

1. Miller, W. O., Gamble, M. T., "Superconducting Super Collider Silicon Tracking Subsystem Research and Development" LA-12029, Los Alamos National Laboratory, Los Alamos, NM, 1990.
2. Special Issue on Acoustic Microscopy, IEEE Trans. *Sonics and Ultrasonics*, SU-32, no. 2, 1985.
3. Krumweide, G. C., Brand, R.A., "Attacking Dimensional Instability Problems in Graphite/Epoxy Structures," Composites, Proceedings of the Eighth International Conference on Composite Materials (ICCM/8), Honolulu, July 15–19, 1991.
4. Thompson, T. C. and Miller, W. O., "Development of Ultrathin, Dimensionally Stable Composites for the Superconducting Super Collider (SSC) Elementary Particle Detectors," Proceedings of the Advanced Composites 1993, International Conference on Advanced Composites, Wollongong, Australia.
5. Chamis, C. C., "Simplified Composite Micromechanics Equations for Hygral, Thermal, and Mechanical Properties," *SAMPE Quarterly*, April 1984.
6. Springer, G. S. and Tsai, S. W., "Thermal Conductivities of Unidirectional Materials," Chap. 2, *Environmental Effects on Composite Materials*, ed. G. Springer, ISBN 087762-300-7.
7. Burland, D., Shattuck, D., et al., "The Thermal Conductivity of Elastomer Composites for Electrophotography," *Journal of Imaging Technology*, **15**:257–263, 1989.
8. Nielsen, L. E., *Mechanical Properties of Polymers and Composites*, Vol. 2, Marcel Dekker, Inc., 1974.

APPENDIX C

DRAFT

GROUP MEE-12

OF THE

LOS ALAMOS NATIONAL LABORATORY

FISCAL YEARS 1992 AND 1993

RESEARCH AND DEVELOPMENT REPORT

Submitted to the

SILICON TRACKING SUBGROUP

OF THE

SOLENOIDAL DETECTOR COLLABORATION

DRAFT

CONTENTS

1.0 INTRODUCTION

2.0 EXECUTIVE SUMMARY

3.0 TECHNICAL DISCUSSION

3.1 Design Description

3.2 Design and Development Activities

3.2.1 Enclosure/Supports

3.2.2 Space Frame

3.2.3 Silicon Shell Development A three dimensional shaded image of the proposed silicon shell structure for the central region is shown in figure xx. This silicon shell assembly is typical of the 12 individual silicon shell structures that comprise the STS central region. Each silicon structure is composed of two graphite fiber/cyanate ester resin composite rings onto which individual silicon detector modules are precisely bonded. The modules are bonded on the inside as well as the outside of the rings, thus, forming two silicon layers on one structure. Two such layers are generally referred to as "super-layers." The composite ring structures are referred to as cooling rings, since they serve a dual function of supporting the polystyrene wick structure. As discussed earlier, the wick structure distributes the liquid butane to each detector for cooling the electronics. The radiation length penalty associated with this ring structure should be charged against the STS

structure budget, since the ring is required regardless of the cooling system approach. Hereafter, we will refer to the ring as a "cooling ring," solely to remain consistent with earlier publications.

Each detector is placed at a 7.4° tilt to a radial line emanating from the detector centerline. This construction feature permits azimuthal detector hermeticity, a shingle-like pattern with detector overlap. This important feature is obtained at some expense to ring fabrication complexity. To achieve the requisite tilt, it is necessary to produce a saw-tooth pattern on the inner and outer surface of the ring.

The STS experimental program has concentrated on the development of a cooling ring for the detector central region. Our investigation into the fabrication and material development issues was initiated on a 42 cm outer diameter ring. We plan to construct an engineering prototype of a 42 cm silicon shell assembly, and conduct stability tests by monitoring shell distortions with TV Holography methods. The subsequent sections deal with the ring fabrication and material developments, shell and ring thermal/mechanical performance predictions, and kinematic mount developments for supporting the completed silicon shell. A semiautomated work station assembly unit is under design for the precision construction of a typical central region silicon shell assembly. The work station will also be used to assemble the flat planar arrays characteristic of the forward regions in the STS. Work accomplished to date in this area is also detailed in subsequent sections.

3.2.3.1.1 Cooling Ring Development

3.2.3.1.2 Materials Considerations

Material studies, cited earlier, have considered thermal expansion, moisture expansion, radiation length, thermal conductivity, elastic modulus, resistance to radiation and chemicals, and manufacturability. On the basis of an optimization of these parameters, the baseline material is P-75/954-3, a high-modulus graphite with a cyanate ester resin system.

The program was configured to start with commercially available molding compounds, then to progress into customized materials with higher moduli, using hydrophobic resin systems. The earlier efforts had more modest goals of achieving wall thicknesses of 450 μm and 30° arc segments.

Using Fiberite MX/4925 molding compound, we found that a shorter fiber length was required in order to achieve good fiber distribution in the mold. Also very exacting distribution of the charge was required to prevent the gelling of the resin due to increased heat transfer from the thin wall. The compounding of the fiber and resin was in a 45/55 weight ratio, respectively. This system was developed specifically for commercial molding, and it worked well, except that

the fibers had to be shortened from 12 mm to 6 mm to get the material to flow in the thin-walled cavity.

Short discontinuous fibers were obviously needed to flow easily in the thin mold cavity wall. Two possible fiber lengths were chosen to continue the development work: 100 μm and 400 μm. It should be noted that short fibers degrade the performance of the composite and the program plan called for using the longest fiber which still produced high quality pieces.

Graphite/epoxy composites have been tested in a radiation environment, and data exist on the aromatic amines (3501-6) and aromatic isocyanates (1939-3). These composites show that structural degradation after exposure to 10 Mrads is not a problem. However, none of the existing data on graphite/epoxy composites explains how dimensionally stable the material will be after being exposed to a radiation environment in the presence of a hydrocarbon, such as we propose.

3.2.3.1.2.1 Ball Milling of Fibers

A critical manufacturing operation for producing thin compression molded parts is the sizing of fiber. Commercial quantities (500 kg) of continuous fiber were shortened to approximately 100 μm length fibers. Since small quanities of material are required for the SSC program, ball milling operations were established at Sandia National Laboratories (SNL) and Programmed Composites, Inc. (PCI). PCI worked on milling lengths of 400 μm and SNL worked on both producing 100 μm lengths but in larger quantities.

The objective was to establish an optimum fiber length which allowed for ease of manufacture (short fiber) and optimum thermo- physical properties (long fiber).

The ball milling at PCI used a small one-quart capacity mill. A well-defined process was worked out with resulting fiber length vs. time shown in Figure 0-1.

Figure 0-1. Fiber length distribution for PCI ball milling operation

A matrix of ball milling parameters was evaluated at SNL to try and establish consistent sizing of the fiber. The ball mill used at consisted of a two gallon container and ZrO_2 balls and a suspension fluid. After many trials of different weight loading of fiber and media, we consistently got our best results with 230 gm of fiber, milling with 30 kg. of ZrO_2 and the container filled to 90% of capacity with Freon.

The dispersion of fiber within the media was critical to achieving repeatable results. Best results were obtained by distributing the fiber between layers of ZrO_2, with each layer being nominally 1/7 of the total. Photos of typical ball milling results from SNL are shown in Figure 0-2. It is interesting to note that although the ball-milled fiber length is function of time that the spread in fiber length is quite large using this process.

Figure 0-2. Typical graphite fiber appearance after ball milling for one hour in two gallon ball mill.

The ball milling operation was not as repeatable in achieving uniform fiber length as sought. It is currently believed that to produce high quality uniform fibers, a new chopping process will need to be developed.

3.2.3.1.2.2 Matched Metal Molding

The manufacturing of the composite rings has taken several evolutionary steps. The first step was to start with commercially available materials and then evolve into the materials that we have baselined for the STS. The original 30° arc was molded using MX4925, which uses an intermediate-modulus fiber, along with a phenolic resin system. Because of the extremely thin wall section, the charge had to be distributed carefully within the mold to enable the compound to move small distances prior to curing. A procedure was developed that produced high-quality 30° arc segments.

This combination of material did not suit our long-term objectives for several reasons. For example, we required an extremely thin wall, which required going to shorter fibers than those commercially available. Furthermore, the resin system was not hydrophobic and, therefore, was not considered to be stable.

In the second phase of the manufacturing development, the 30° arc segment was extended to 120°, and we used the materials we had baselined for the other structural components. The geometry was also modified to reflect the latest physics requirements, and the wall thickness was reduced to 400μm. The compression mold was equipped with several new features to improve moldability. These features included the use of air ejection to release the part from the mandrel, and the grip features, which could easily be attached to automate the opening and closing of the mold while in the press.

The mold was manufactured from A2 tool steel, which is typical for this type of mold. The quality was quite good, and the tight tolerances were held. Figure 0-3 shows half the tooling which was used. The only deviation from the specification was in the wall thickness. The mold had a slight offset that could not be taken out easily. It was therefore decided to use the mold as received from the manufacturer. The inside wall thickness was nominally 380 μm, while the outside wal thickness was 420 μm.

Figure 0-3. Male portion of the matched mold tooling

The second molding compound was a Fiberite product, ICI CF90. This higher modulus fiber came in 90-μm-fiber lengths. The resin system was TEM9000, a toughened epoxy system

from Fiberite, made for production of high-quality graphite components. Three different resin batches were evaluated: 40%, 50%, and 60% matrix filler by weight.

The resin's viscosity was high and the cooling ring could not be satisfactorily molded if the resin content fell below 50%.

The next iteration of material was to incorporate the high-modulus P-75 fiber with the TEM9000 resin. This combination produced good quality components as long as the resin weight content remained above 50%. A substantial amount of work was put into developing the mold-ability of the 40% resin combination, i.e., withe the desired high fiber fraction, but with little success. Figure 0-4 shows a typical micrograph of a cross-section of a cooling ring in a defective area. The time, temperature, and preheat cycles were all varied with little improvement. Thus, the viscosity could not be lowered enough to move the material around in the extremely thin wall mold. It may be possible, with further development, to get this system to work, but the accelerator that is used for commercial components in the epoxy system would need to be removed.

Figure 0-4. Cooling ring cross-section, 40% epoxy, 60% P-75 graphite fiber by weight showing manufacturing difficulties

The next iteration of material was the incorporation of the toughened cyanate ester based resin system, Fiberite 954-3. This system's viscosity is approximately 100 times lower than that of the TEM9000 epoxy. Two systems were tried, 40% and 50% resin. Both systems had a low enough viscosity to flow easily within the mold.

Cyanate ester is an excellent adhesive, and no commercial mold releases we tried were successful in releasing the arc segment from the mold without breakage. A TEFLON base coat, Dupont 850-314 with a thermoplastic Dupont PFA Powder Coat 532-5010 was finally found to work. The mold was coated with this system, and we successfully released the molded part from our mold.

The last issue to be resolved was the fragility of the P-75/954-3 system. The molding compound was not as robust as the TEM9015, and it was very susceptible to breakage if the standard mold cycle was followed. If the component was removed after 30 minutes instead of 2 hours, the part was compliant enough to survive the two mold halves coming apart. It was now necessary to use a post curing mandrel to finish the cure cycle.

3.2.3.1.2.3 Hard Rubber Molding

A second parallel path was being developed at SNL and PCI. Because of the difficulty and cost associated with matched metal molds, a spray process was being worked out to spray the Gr/resin system directly onto the mandrel. If such a system could be developed, it would

eliminate the high program costs of matched metal molds and solve the problem of uniform material properties in the plane of the composite.

Different diluents were evaluated to see which carried the compound with minimal interaction with the epoxy. Our earliest success came by using acetone as the diluent. This had a pot life of a couple of days and provided even distribution and excellent adhesion to surfaces in any direction.

Test articles were prepared over a flat plate to demonstrate if the Graphite/resin system could be sprayed effectively then consolidated under pressure and temperature. The results are shown in Figure 0-5 for both standard material dispensing and the sprayed concept. It can be readily seen that the fibers from the sprayed process does exhibit a more random particle distribution that a standard charge dispensing technique.

Figure 0-5. Photomicrographs comparing the fiber orientation of sprayed versus standard charge dispensing

We were encouraged by the improvement in material orientation enough to continue the development process. The next step was to try and spray over the actual male mandrel and then consolidate the constituents under pressure.

The first attempt of using the hard rubber mold resulted in nonuniform part thickness. The mold consisted of a male mandrel with a hard rubber over press approximately 2.5 cm in thickness and two sturdy outer aluminum shells, as shown in Figure 0-6. This configuration did not develop enough pressure at 175°C to uniformly consolidate the the Graphite and produce a high quality part. Work is continuing at PCI in increasing the pressure by using TEFLON inserts in place of the hard rubber.

Figure 0-6. Mold used in the spray deposition process

3.2.3.1.3 Thermal Conductivity Enhancement

Chopped fiber/resin compression-molded products are theoretically quasi-isotropic. However, long fibers, e.g., greater than 6 mm when compression molded into ultra thin shapes, will be forced to be parallel to the mold wall. Both the resin and the transverse fiber thermal conductivity is low; hence, thermal conductivity through the wall cross section is also quite low, $< 1 W/m\text{-}K$. In this application, it is important to minimize the thermal gradient from the electronics to the cooling system's evaporative wick structure; this requires a minimum gradient through the ring wall. If the gradient were not minimized, the silicon strip detectors would operate considerably above the desired 0°C. We have investigated means of enhancing the transverse thermal conductivity of the composite cooling ring, as well as loading adhesives with high thermal conductivity particles.

The thermal gradient through the cooling ring was predicted using properties for the composite thermal conductivity (both transverse and in-plane), and the evaporative wick-film coefficient. Finite element (FE) solutions were obtained as a function of transverse thermal conductivity (k_t) for a constant heat flux. This solution isolated the thermal fin effect of the cooling ring sidewall. For a low kt, (e.g., 0.7 W/m-K characteristic of the MX4952 carbon/phenolic system), heat flows down the ring sidewall, as well as through the top surface of the ring. The results of this study clearly identified the benefit of achieving a k_t of 4 W/m-K in the transverse direction.

Our first approach in enhancing the transverse composite ring thermal conductivity was to fill the resin system with particles. At the onset, we did not appreciate the extent to which the introduction of particles would enhance the kt in a composite ring, or interfere with ring's moldability. We knew that the complex ring geometry required compression molding with fiber lengths much shorter than standard chopped prepreg material. The structural aspects of the ring design also dictated a high-fiber volume fraction; consequently, the volume fraction of particulates in the resulting matrix would be quite limited. We experimented with resin loaded with an additive, resin filled with a combination of discontinuous randomly oriented, graphite fibers and particulates. We compared our results with those from other related work to form a basis for future development effort. Our filler additive study was confined to aluminum nitride and diamond particles.

The thermal enhancement of aluminum nitride spherical particles in a cyanate ester resin system is shown in Figure 0-7. The thermal conductivity was evaluated for discrete volume fractions up to a maximum of 27%. Specimens were cut from 3.1 mm compression molded disks (500 psi), and tested by a standard laser flash diffusivity technique to obtain the thermal conductivity. These results were compared with experimental data published by Bujard (Ref. 1).

Figure 0-7. Thermal conductivity enhancement factor, k_{ef}, of filled cyanate ester resin.

Bujard developed the curve in Figure 0-7 using the Lewis-Nielsen model to fit the measured thermal conductivity data. The Nielsen model can be in terms of an enhancement factor k_{ef}, where:

$k_{ef} = k_s/k_m = (1 + ABV_f)/(BYVf)$ and (1)

k_s = sample thermal conductivity;

k_m = neat resin thermal conductivity;

k_f = filler thermal conductivity;

$B = (k_f/k_m - 1)/(k_f/k_m + A)$;

$Y = 1 + ((1 - f_m)/f^2m)V_f$;

A = factor depending on particle geometry (1.5 for spherical particles);

V_f = filler volume fraction; and

f_m = maximum volume ratio obtained

from sedimentation experiments.

Bujard obtained a best fit to the data using the shape factor A of 8, with a particulate thermal conductivity of 6 W/m-K, which he indicates is representative of "particle clusters." The 6 W/m-K contrasts with the intrinsic thermal conductivity of aluminum nitride, which is 280 W/m-K. He also obtained a maximum packing fraction limit of 0.62. Bujard concluded that the high shape factor of 8, versus a value of 1.5 for spherical particles, was a consequence of the formation of thermally conductive clusters and could be explained through bond percolation theory.

A predicted curve extracted (Ref. 2) is also depicted in Figure 0-7. This model originates with Sheng (Ref. 3). Sheng's predicted curve is for randomly oriented spherical particles with a filler-to-resin thermal conductivity ratio of 100. Reference 2 also shows that when this ratio exceeds 50, very little further increase in thermal conductivity enhancement is obtained. This observation is also true of the Nielsen model, where the parameter B approaches 1, and thereafter the magnitude of the particulate material thermal conductivity plays only a minor role. Since in the ratio of intrinsic aluminum nitride to C-E resin thermal conductivity is well above this criterion, we were able to use the prediction by Sheng directly. It should be noted that this curve agrees reasonably well with our data. One may conclude that in our compression molding of specimens, we did not obtain any significant "thermally conductive clusters" that effectively spanned the material thickness, but, more likely, a more random distribution of particles. A good correlation exists with our data by reducing the geometry factor A from 8 to 1.5, representative of spherical particles as cited by Bujard and others. At the low volume fraction tested, the effect of bond percolation was not evident.

A second sampling of material specimens was produced with the addition of 100-μm-long P-75 fibers to the matrix. The actual fiber length distribution was rather asymmetric, ranging from 90 to 600 μm, with 100 μm representing the nominal length. Specimens with various volume fractions of particulates and fibers were produced. The volume fraction of solids ranged from 45 to 56%. A thermal conductivity enhancement ratio was formed by normalizing the composite property to that of the neat resin. We chose to plot this enhancement ratio as a function of the volume fraction of P-75 fibers, the most dominant solid matrix fraction. Figure 0-8 shows this enhancement ratio with the various volume fractions of particulates denoted as a secondary parameter.

Figure 0-8. Thermal conductivity enhancement factor k_{ef} of P-75 fiber and particle filled cyanate ester resin.

References 4 and 5 contain several theoretical models for the transverse thermal conductivity of continuous graphite fiber/resin systems. The simplified model by Chamis (Ref. 5) contains the following expression:

$k_{122} = k_{tf} k_m$, where (2)

k_{t22} = composite transverse thermal conductivity;

k_m = neat resin thermal conductivity, and

k_{tf} = transverse thermal conductivity enhancement factor

$$k_{tf} = (1 - V_f) + (\sqrt{V_f}) / \left(1 - \sqrt{V_f}(1 - k_m/k_{f22})\right)$$

and,

V_f = fiber volume fraction, and

k_{f22} = fiber transverse thermal conductivity.

The above expression accounts for the fiber transverse thermal conductivity k_{f22} that is typically an order of magnitude lower than the fiber longitudinal kf11. As before in the particle filler case, it can be shown that once the thermal conductivity reaches a value of 50, little further benefit is gained by introducing fibers that possess a higher k_{f22}.

Springer's (Ref. 6) expression for the transverse thermal conductivity agrees remarkably well with the Chamis expression. Springer's model, however, does tend to predict more of an increase in overall kt above a volume fraction of 0.6 than does the Chamis model. Intuitively, this effect seems reasonable. Referring to Figure 0-8, the experimental data are distinctly above the predicted Chamis fiber-only curve. One data point for the very large volume fraction of spherical diamond particles (30%) is noticeably higher. For comparative purposes, Bujard's curve for the aluminum nitride has been added to Figure 0-8. For high-volume-fraction particulates and lower volume fraction fibers, some correlation with the particulate-only curve exists. Thermal clusters of particulate matter, which span the material thickness, now seem to exist for this composite.

Several cooling ring arc segments were produced with aluminum nitride and graphite fibers (11% AIN by vol., 39% fiber). The transverse thermal conductivity agreed with the compression-molded disc data, although the ring section was much reduced in thickness, 0.5 mm versus 3 mm. We observed that molded rings with combined solid volume fractions over 50% were brittle. This test series ruled out molding a composite ring from two solid constituents.

At this juncture, we realized that the aspect ratio of the particles was extremely important to attaining high thermal enhancement ratios. Two options appeared to be open. First, the investigation could be repeated using hexagonal boron nitride particles that evidently produced very effective thermal clusters (Ref. 6), or we could redirect the study's efforts toward achieving a random distribution of fibers. The 100-μm-long fibers are similar to particles whose aspect ratios are 10. We chose to continue our investigation solely with fibers, and expand the study to include 400-μm-long fibers, yielding a nominal aspect ratio of 40. The 400-μm-fiber length was chosen as a means to span the ring's wall thickness and to use their high fiber thermal conductivity property to enhance the kt.

Figure 0-9 illustrates the measured transverse thermal conductivity for cooling rings with 60/40 volume fraction. Thermal conductivities very near our design goal were obtained. We

observed that the kt data for composite ring specimens produced with 100- μm-long fibers were decidedly lower. As a further comparison, thermal conductivity data obtained with the early MX4925 carbon/phenolic molded ring with relatively long fibers is included. These data tend to agree with the Chamis prediction for long-fiber composites.

Figure 0-9. Transverse thermal conductivity of 450 μm thick cooling ring segments from compression molded cyanate ester/P-75 discontinuous fibers (100,400μm) as function of fiber volume fraction.

The Sheng model prediction for a randomly oriented prolate ellipsoid particle ("needle-like") with an aspect ratio of 10 is depicted in Figure 0-9. This aspect ratio conforms to our 100-μm-long fiber. Reference 2 also has similar predictions for the long axis of ellipsoidal particles oriented normal to the direction of heat flow. For this case, the predicted thermal conductivity is similar in magnitude to the Chamis model at volume fractions less than 40%. For higher volume fractions, the Sheng model predicts considerable enhancement. This model for the random orientation predicts a higher enhancement, as evident from our data; however, our fibers are far from being random.

3.2.3.1.4 Fiber Length and Resin Volume Fraction Considerations

As in the case of the cooling ring thermal conductivity enhancement investigation, the Lewis and Nielsen model can be used to characterize the elastic modulus as a function of fiber aspect ratio and volume fraction. The general expression for the modulus ratio, i.e., the composite modulus to the unfilled resin modulus, is of the same form:

$$\frac{M}{M_1} = \frac{(1 + ABV_f)}{(1 - B\Psi V_f)} \tag{3}$$

In the foregoing expression, M can be any modulus, i.e., shear, tensile, or compressive. The constant A is a simple multiple of the fiber aspect ratio for uniaxial orientation of the fibers, whether they be continuous or discontinuous. For a longitudinal elastic modulus case, El, A becomes:

$$A = 2L/D = 2\mathrm{AR} \tag{4}$$

and L and D are fiber length and diameter respectively, and AR is the fiber aspect ratio.

The expression for B is of the same form as before, except it now contains the ratio of the fiber modulus to resin modulus in place of the material thermal conductivities. Again, B is expressed as:

$$B = (E_f/E_m - 1)/(E_f/E_m + A) \tag{5}$$

where E_f and E_m are the fiber and resin Young's modulus respectively.

Factor y takes into account the volume fraction of the fibers. The expression, as before, is:

$$= 1 + ((1 - f_m)/f_m^2)V_f \tag{6}$$

Here the value of f_m is the maximum packing factor for the fibers. The fm varies with particle shape and state of agglomeration. It is difficult to predict f_m from theory. It is generally experimentally determined from sedimentation measurements or from the maximum packing of dry particles, or fibers, under vibratory motion. For fibers, Reference 11 gives the following values for cubic packing, 0.785; and hexagonal, 0.907.

In general, random close packing will lie between these limits. For our study we chose 0.82 as an initial value in correlating with composite test data.

It is possible to generate a figure depicting Young's modulus (tensile) for the composite as a function of fiber aspect ratio and volume fraction for longitudinal fiber orientation. The result is shown in Figure 0-10 in a non-dimensional form for fiber and resin properties corresponding to P-75/Cyanate Ester. At a fiber aspect ratio of 1000, the modulus ratio for 60% volume fraction is 82.11, which is approaching a continuous unidirectional fiber matrix. Extrapolating out to Ar = 10,000, the modulus ratio becomes 83.6. For the cyanate ester resin, we established a tensile modulus of 3.7 GPa; consequently, the predicted composite modulus for the long fiber (0.1 meter) would be 309.3 GPa (Nielsen model). The value is in rather close agreement (3.9%) with our measured value of 321.3 GPa. It is possible to see from Figure 0-10 the strong dependence of modulus on fiber aspect ratio. To realize the stiffness of an unidirectional composite, the aspect ratio clearly must be greater than 100.

Figure 0-10. Ratio of longitudinal composite modulus of elasticity (El) for P-75/954-3 to matrix modulus (Em).

It is also clear from this figure the importance of obtaining a high fiber volume fraction. For an aspect ratio of 100, 60% fiber fraction produces a factor of 1.7 greater stiffness over 40%. The improvement in stiffness also is apparent at lower fiber aspect ratios. Achieving high fiber volume fractions has been our goal from the onset. The Nielson model affords an opportunity to qualitatively assess this factor.

In the case of our composite cooling ring, we are using fiber aspect ratios on the order of 10 to 40, and fibers are randomly oriented. The above figure cannot be used to predict the stiffness behavior for such a complex matrix. However, Reference 11 recommends a method for adjusting the predicted curves for the individual situations of two and three dimensional randomly oriented fibers. The expressions for these two cases are:

$$E_{2d}/E_m = (3/8E_l/E_m + 5/8E_T/E_m) \qquad \text{2-dimensional} \tag{7}$$

$$E_{3d}/E_m = (1/5E_l/E_m + 4/5E_T/E_m) \qquad \text{3-dimensional}$$

To evaluate the transverse modulus ratio (E_T/E_m) required by these expressions, the same procedure is used as before, except the value of A becomes constant 0.5. The predicted results derived from these expressions are shown in Figure0-11. We chose not to use a non- dimensional format in order to provide a direct comparison with our composite cooling ring structural test investigation.

Figure 0-11. Composite Modulus (E) versus fiber aspect ratio, for both 2D and 3D randomly oriented fibers for 60% and 40% fiber volume fractions.

Measured values of elastic modulus for specimens extracted from the compression molded cooling ring (P-75/cyanate ester resin) are shown in Figure0-11. The data is plotted at a nominal aspect ratio of 10, corresponding to a fiber length of 100 μm. Acid digestion tests placed the fiber volume fraction at nominally 45%, considerably below our goal of 60%. It is difficult to estimate to what extent the composite approaches a highly 3 dimensional matrix. A review of the ultrasonic Non Destructive Evaluation (NDE) measurement suggest that the composite tends to be 2-dimensional, i.e., more fibers are oriented in the plane of the cooling ring wall. We observed from these measurements that much of the fibers were less than 100 μm.

One may note that at an aspect ratio of 1000 that the elastic modulus has a definite positive slope. Extrapolating the modulus calculation out another order of magnitude (A_r = 10000) yields for the 2-dimensional prediction a value of 118 GPa. This value is close to 98 GPa we measured on quasi-isotropic continuous fiber coupons. Although our study is far from complete, it would appear that the Nielsen model for elastic modulus can provide a reasonable approximation for a domain ranging from discontinuous to continuous fibers.

3.2.3.1.5 Non Destructive Evaluation

Ultrasonic techniques were used to evaluate the material variation and mechanical properties of the cooling ring. This evaluation was used to assess the manufacturing development of the cooling ring. The techniques being used include pulse-echo scanning techniques and time-of-flight measurements.

The intensity of an incident ultrasonic wave that reflects and transmits at a material interface is governed by the materials acoustic impedances, which is the density of the material multiplied by its acoustic velocity. For a composite composed of many material interfaces, a measure of the transmitted and reflected intensities by well known pulse-echo techniques is an efficient measure of the qualitative uniformity of the composite. These techniques are quick and make for efficient evaluation of the manufacturing parameters. Volume fraction variations of the fiber/matrix, as well as voids or resin poor areas, are easily detected. The images that result from spatial variations in the acoustic impedance is well documented in the published literature (Ref. 8).

Macroscopic and microscopic material composite variations were imaged for the composites of this study. A typical pulse-echo amplitude plot of the full thickness echo is shown, in Figure0-12, using a 30-MHz focused transducer. The image of Figure 0-12 indicates a uniform composite except for the resin rich area indicated in black on the right side of the image. Normally, a pseudocolor image is generated,but for this paper the images were reproduced with a gray scale image. The vertical line was due to an imperfection in the mold surface. The images of Figure 0-13 show the pulse-echo amplitude variations for four test pieces representing different manufacturing options. The light gray areas in Figure 0-13 show where high amplitude pulse-echo signal were obtained. The dark areas show where high attenuation of the signals occurred, indicating poor material interfaces between fibers and matrix or an increase in thickness. A uniform color would indicate a homogeneous composite composition. The variations shown in Figure 0-13 indicate a less desirable fiber composite uniformity.

Figure 0-12. Image of pulse-echo amplitude variations indicating where compositional changes occur within the composite.

Figure 0-13. Images of the pulse-echo amplitude variations for four test pieces for several different manufacturing options.

A scanning acoustic microscope (SAM) was used to image the reflection intensities due to variations of the surface constituents of the fiber composite on a μm scale. The SAM used in this study was an Olympus UH3 acoustic micrscope. Figure 0-14 shows a mosaic of the cooling ring composite where the distribution of the fibers is clearly observed. These images were obtained with a 400 MHz focused transducer.

Figure 0-14. Mosaic of SAM images taken at 400 MHz of the cooling ring composite.

The distribution of the fiber and particulate composition for the four test pieces of different manufacturing options are shown in the SAM images of Figures0-15 and 0-16. The images of Figure 21 show that only a few 400-μm fibers are present in the composite. Many much shorter fibers are present than is desired. This is also reflected in the low in-plane moduli values measured for these composites shown below.

Figure samii. SAM images of (a) Holometrics 400-μm test piece and (b) PCI 400-μm test piece.

The SAM images of Figure 0-16 show that the LANL 1 and Holometric 100-μm test pieces contain longer fiber distributions and, as a result, higher moduli values are measured.

Figure samiii. SAM images of (a) LANL 1 test piece and (b) Holometrics 100-μm test piece.

Time-of-flight measurements were obtained by contact through-transmission buffer rod techniques and liquid immersion through-transmission techniques (Refs. 9 and 10). Acoustic velocities were calculated from the time-of-flight measurements in the principal axes of the composite, and

with a density determination, the elastic constants and engineering moduli were computed. The results of the moduli calculations are shown in Table 0-1.

Table0-1. In-plane (1) and Out-of-plane (3) Elastic Constants and Young's Moduli

Sample	C11[a] (GPa)	C33[a] (GPa)	E1[b] (GPa)	E3[b] (GPa)
LANL 1	25.1	20.8	22.3	20.5
PCI 2	17.8	16.7	15.3	14.0
Holometric 400 3	19.4	13.9	14.0	11.4
Holometric 100 4	22.3	13.4	15.7	9.7
Holometric 400 5	19.1	12.3	14.8	8.3
50/50	25.1	15.4	17.7	9.3
Quasi-isotropic	266.5	11.2	97.6[c]	3.5

[a] Longitudinal Moduli C11 and C33 are obtained by multiplying the density by the velocity squared where 1 is the in-plant velocity direction and 3 is the thickness direction. These measurements are easy to make. They provide a quick measure of the elastic property characterization of the material.

[b] E1 and E3 are obtained by making longitudinal and shear velocity measurements in the principle directions and at a 45° direction to the thickness direction. These measurements are more difficult to make.

[c] For the quasi isotropic sample, E1 was 99.3 GPa average over 5 samples by mechanical tests.

Table II also lists the moduli measured for a 50/50 volume fraction sample of 400 μm fibers and a long fiber quasi isotropic tensile sample. The 50/50 sample showed the proper mixture of 400-μm fibers. The quasi-isotropic sample was manufactured with many alternating plies of long fibers resulting in a thick layered sample of 62.2% fiber volume. These two samples are listed as a comparison to the high moduli obtainable with an ideal manufacturing process.

References 1. P. Bujard and J. P. Ansermet, Thermally Conductive Aluminum Nitride-Filled Epoxy Resin, Ciba-Geigy Limited, Research Center, 1701 Friborg, Switzerland.

2. D. Burland, D. Shattuck, and J. Perrin, "The Thermal Conductivity of Elastomer Composites for Electrophotography," *Journal of Imaging Technology* 15:257–263 (1989).

3. P. Sheng, "Theory for the Dielectric Function of Granular Composite Media", *Phys. Rev. Lett* 45:60–63 (1980); "Microstructure and Dielectric Properties of Granular Composite Films," *Opt. Laser Tech.* 13:253–260 (1981).

4. C. C. Chamis, "Simplified Composite Micromechanics Equations for Hygral, Thermal, and Mechanical Properties," *SAMPE Quarterly*, April, 1984.

5. G. S. Springer and S. W. Tsai, "Thermal Conductivities of Unidirectional Materials," Chap. 2, *Environmental Effects on Composite Materials*, Edited by G. Springer, ISBN 087762-300-7.

6. P. Bujard, "Thermal Conductivity of Boron Nitride Filled Epoxy Resins: Temperature Dependence and Influence of Sample Preparation," Ciba-Geigy Limited, Research Center, 1701 Friborg, Switzerland.

7. S. Seehra, et al., "Effects of Space Environmental Conditions of Graphite Epoxy Composites," *SAMPE Journal*, March/April, 1985.

8. Special Issue on Acoustic Microscopy, *IEEE Trans. Sonics and Ultrasonics*, SU-32, no. 2 (1985)

9. J. H. Gieske and R. E. Allred, "Elastic Constants of B-A1 Composites by Ultrasonic Velocity Measurements," *Experimental Mechanics*, 1974, no. 3:158–165

10. T.-T Wu and Z.-H. Ho, "Anisotropic Wave Propagation and Its Applications to NDE of Composite Materials," *Experimental Mechanics*, 1990, no. 12:313–318

11. Lawrence E. Nielsen, *Mechanical Properties of Polymers and Composites*, Vol. 2 (1974 by Marcel Dekker, Inc.)

3.2.3.2 Silicon Detector Prototype

3.2.3.3 Kinematic Mount Design and Development

3.2.3.3.1 Requirements

As the temperature of the detector is reduced to its operating level, components having different coefficients of thermal expansion will undergo dimensional changes that could result in undesirable stresses or displacements. Similar conditions could be caused by asymmetric thermal loading of the silicon structure cooling system. In any case, it is desirable to support the sensitive components of the detector in a manner that allows nearly strain-free thermal expansion and contraction. With the exception of the forward region planar arrays, components requiring this type of support are generally cylindrical in shape. Since stability in any orientation is necessary, the ideal strain-free kinematic mount for the latter can not be implemented, and some compromises must be made. The planar arrays, on the other hand, can easily be supported at three points in a nearly strain-free manner.

Since the most difficult components to support are the central region silicon shells, it is reasonable to assume that a solution to this problem can easily be extended to the support of

composite shells and forward region arrays by the space frame. In the central region, a support system is complicated not only by the shape of the silicon shell, but also by the assembly of individual shells with the composite shell. Because several silicon shells are mounted in tandem, both inside and outside the composite shell, access to the innermost mounts is severely limited. In order to assemble both sets of silicon shells on a composite shell it is necessary to assemble and align either the inner or the outer set first, then remove that set so that mounts for the other set are accessible. Hence, the capability to uncouple the individual mounts from a silicon shell without disturbing their alignment is needed. This is particularly important if failed components (e.g., individual silicon detector strips) are to be replaced in a timely manner during routine maintenance operations. Because interchangability of detector strips and silicon shells is necessary, and the tolerances to which these components are fabricated must be practical, the mounts themselves should be adjustable.

3.2.3.3.2 Mounting Concepts

With these criteria in mind, several mounting concepts are being studied. The first concept is a classical 2-2-2 mount. In its simplest form, this concept consists of three co-planar balls, equally spaced around the periphery at one end of a silicon shell, with each ball resting in a radially -oriented vee groove seat. In this configuration the seats, which are attached to the composite shell, allow only symmetric radial movement of the shell. A set of balls in a similar configuration, but resting on flat, compliant surfaces oriented tangent to the cylinder, are located at the opposite end of the shell. With this mount geometry two axial restraint methods are possible; first, by lightly clamping the balls in the vee grooves, and second, by tilting the flat surfaces at the opposite end so an axial component of force exists. The first axial restraint method has the disadvantages of potential overconstraint due to the radial loads imposed by the flat surfaces or, underconstraint which would result in cantilever support. The second axial restraint method has less of a potential for overconstraint, but would impose axial compressive loads on the entire shell. Neither of these conditions is desirable. Theoretically, the major advantage of the 2-2-2 mount is its ability to produce very symmetric expansion and contraction in a cylindrical geometry. In practice, the mount has the potential for stick-slip, or "stiction" problems due to external friction.

The second, and most promising concept being studied is the tangent bar. As its name implies this device is a flat , compliant strip oriented tangent to the silicon shell. A spherical surface, or ball, mounted on the shell rests on the tangent bar, which is attached to the composite shell. The rest feature for the ball on the tangent bar can be a flat, groove or conical detent. With some initial deflection of the strip when mounting a silicon shell, a preload can be effected that will accomodate radial expansion or contraction of the shell without decentering. Several

combinations of the flat, groove, and detent features are the subjects for upcoming tests on two tangent bar designs. The first combination consists of three equally spaced tangent bars around each end of the silicon shell. All six bars allow radial movement of the silicon shell by virtue of their flexibility. At one end of the shell, the set of bars includes a flat, a groove, and a conical detent. By orienting the groove parallel to the axis of the shell, the shell is locally unrestrained in the axial direction, but is restrained from rotating about it's axis. The bar with the conical detent prevents all but the radial movement, and the third bar, which is flat, merely constrains the shell against the other two. At the opposite end all three bars have flats, thus, free movement in five degrees of freedom and limited movement in the radial direction is allowed. The principal advantage of this arrangement is that none of the balls on either end have to be coplanar or precisely aligned in the axial direction in order to meet the shell's most stringent position tolerance of 5 μm. The shell's position with respect to skew is set by adjusting the radial positions of the bars at the end opposite that of the conical detent. These bars must be positioned radially within 5 μm to meet the requirement, regardless of shell diameter. The major disadvantage of this arrangement is that the constraint is asymmetric and, therefore, the structure has the potential for asymmetric distortion as it contracts and expands.

A variation of the above configuration is one in which all three mounts at one end of the shell are conical detents and the ones at the opposite end are flats. Because of its symmetry and complete axial fixity at one end, this geometry ensures symmetric radial movement, and uniform axial contraction and expansion relative to the fixed end. Its major disadvantage is that the shell's position with respect to skew is set by the accuracy with which the detents are placed. The tolerance in this instance is directly proportional to the shell radius. For example, for the smallest silicon shell to meet the 5 μm requirement , the axial position of the detents relative to the shell (or balls) must be within 5 micron, but for the largest shell this tolerance is about 13.5 μm.

3.2.3.3.3 Three-Axis Adjustable Mount

Figure 0-17 shows a tangent bar mount with adjustment capability in three orthogonal directions. In the figure, the X, Y, and Z directions correspond to the tangential, radial, and axial directions on a typical central region shell, or on a forward region planar array. The adjustment compliance mechanism is a set of three parallelograms that form an enclosed box structure. Two parallel sides of each parallelogram are thin compliant strips, or flat blade flexures. The other two sides are rigid plates. When one rigid plate is fixed and a force is applied to the other in a direction normal to the plane of the flexures, the flexures behave as a pair of elastic beams with the free ends guided. For small displacements, the resulting motion is essentially linear and parallel to the fixed plate. In this design, the three stages are considered to be tandem; that is,

the Z stage, which carries the tangent bar, is carried by the X stage, which in turn is carried by the Y stage. The stages are stacked in this manner because the Y, or radial direction is the one in which the mount must move when disengaging from the shell. The number of stages required on any given mount is determined by the tangent bar rest feature. A conical detent bar requires all three stages , whereas the groove needs only the Y and X stages, and the flat needs only the Y stage. It is also possible for a groove bar to have a Z stage instead of the X stage. The tangent bar itself is simply a wide, flat flexure with its ends fixed and a stiff section at its midspan for the rest feature. When a normal force is applied at the rest point, such as the preload mentioned above, the flexure behaves somewhat like a pair of elastic beams with the free ends guided.

Figure 0-17. This figure needs a caption.

3.2.3.3.4 Materials of Construction

Compliant members, or flexures, are ideal devices for the mount structures because their mechanical behavior is quite predictable and they perform in a smooth, frictionless manner with no backlash. They are, however, subject to relatively large strains that result in high stresses. In this design, for example, the diplacements of the XYZ stages range from 0.50 mm to 1.25 mm with corresponding normal stresses ranging from 190 MPa to 370 MPa. Stresses in the tangent bar itself are also in this range. Although there are a number of excellent high strength materials

available for flexure construction, most of the more desirable ones must be used sparingly or avoided altogether because material volume and density must be minimized in this application. Commonly used materials, such as 17-4 PH stainless steel, beryllium copper, and Ni-Span C all have yield strengths in the range of 1040 - 1380 MPa, but their densities are about 3 times higher than is acceptable. Wrought beryllium has the most desirable density (1.85 g/cm^3), but its yield strength is only about 276 MPa. The material best suited for the bulk of the mount construction is aluminum alloy 7075 in the T6 condition. Its yield strength is about 520 MPa and its density is 2.7 g/cm^3.

Although most of the mount assembly can be made of aluminum, it may be necessary to use harder high strength materials for components subjected to concentrated loads. The worst case for this kind of loading in the mount occurs at the interface of the spherical feature on a silicon shell and the flat on a tangent bar. Because the load is concentrated at a point, the Hertzian (contact) stresses, which depend on the radius of the spherical surface and the material properties, can be extremely high. For example, if a 4.45 N force is imposed on the interface, and the spherical radius varies from 2.0 mm to 7.0 mm, the resulting compressive stresses range from 1400 MPa to 600 MPa for steel components. It should be noted that the largest silicon shell will impose a total force of about 14 N on the mount system due to it's weight alone, that is, neglecting any flexure preload. Harder, wear resistant materials are needed to prevent wear patterns that may develop with time due to thermal cycling. While these patterns may not upset the 5 μm position requirement because of the preload on the flexure, they would make realignment very difficult if not impossible. Dimpling or peening of the surfaces due to local yielding would cause the same problem. Materials best suited for the mount interface components include 17-4 PH and 440C stainless steels. The latter has a yield strength of about 1900 MPa and a hardness of 57 Rockwell C, whereas 17-4PH has a hardness of 44 Rockwell C. By comparison, 7075-T6 aluminum has a Brinell hardness of 150, which is roughly zero on the Rockwell C scale. Oxides such as alumina or beryllia are harder than 440C stainless, but have relatively low tensile strengths (193 MPa and 138 MPa, respectively). Under the conditions described above for the steel example, the maximum radial tensile stresses range from 277 MPa to 120 MPa. Clearly, the oxides have the greatest potential for failure in tension.

3.2.3.3.1 Mount Adjustment

The most difficult devices to implement in the mount design are the prime movers for the stage adjustments. These devices must be capable of positioning the stages within 5 μm, and still have relatively large load carrying capacities, a combination that can be difficult to implement. To ensure stability of the mount after it has been adjusted, it should be possible to lock the stages with simple clamping, or the flexures should be stiff enough to prevent drift. While it is possible to clamp the X and Z stages, the Y stage will most likely have to depend on flexure stiffness for it's stability because of the uncoupling requirement. The flexure for this stage must be stiff enough to ensure a suitable fundamental natural frequency for the shell assembly. Also, it should be stiff enough to be insensitive to the tangent bar preload. If clamping is used to lock a stage, the force applied must be orthogonal to the direction of adjustment. Clamping schemes using opposing forces in the direction of the adjustment for micron level of accuracy are not feasible.Threaded devices such as differential screws and screw-driven wedges typically suffer from manufacturing imperfections that result in backlash and roughness of motion. Some of these problems can be overcome by single-point turning of threads, lapping of mating parts, and vapor deposition of durable dry lubricants such as tungsten disulfide.

Since the prime movers are used only to precisely control the position of the mount during assembly, and not necessarily to provide any operational stability, it may be feasible to use a removable setup fixture that carries the prime movers only. In this concept, it is conceivable that commercially available micrometer/piezoelectric devices could be used to achieve accuracies on the order of several microns. The micrometers would be used to coarsely position the piezo-electrics, which would then be used to drive the mount stages. After the adjustments are made, and the stages or flexure motion stops fixed by clamping, the fixture with the movers would be removed. This concept also has the potential for reducing the amount of unwanted material in the detector. It should be noted here that this concept for positioning the mount stages is quite new and has not been studied in any detail. Problems concerning mount accessibility during assembly, and mount stability during stage locking need to be investigated. It is important to note also that this concept is for positioning the mount on the silicon shell, not for adjusting the the position of the latter. It is assumed that the shell itself is supported, positioned, and held stable by a completely independent device during the mount engagement operation. Regardless of the assembly procedure it is imperitive that distortion of the silicon structure be monitored during the procedure if alignment is to be maintained and deformations controlled.

3.2.3.3.6 Prototype Testing

Early in the coming fiscal year, the first of what is expected to be a series of prototype tests will be performed to determine certain characteristics of the adjustable tangent bar mount. Of particular interest are the mount's adjustment precision and manageability, its long term stability, and its behavior during thermal cycling. For the initial tests the mounts, which will be made primarily of 7075-T6 aluminum, will include various combinations of X, Y, and Z adjustments with the flat, cone and groove tangent bar features. A cylindrical aluminum shell, similar to one of the smaller central region modules in size and weight, will be used to represent the silicon structure in the these tests. Later tests will include an actual silicon module.

3.2.4 Silicon Shell Analysis Until recently, only greatly simplified or partial models of the detector's silicon structures were used to evaluate thermal and mechanical characteristics using the finite element method. Now a more extensive model of a complete central region shell is used to calculate a structure's response to various thermal loads, its static gravity sag with different support conditions, and its natural frequencies. The current finite element model and results of these analyses are discussed in this section.

3.2.4.1 Model Description The current finite element model represents the second shell in the central region assembly. This shell has an inner diameter of 360 mm, an outer diameter of 420 mm, and a length of 240 mm. Each composite cooling ring is modeled as a hollow shell with a cross section 8 mm wide by 30 mm high, and a wall thickness of 0.40 mm. To simplify the representation of the silicon strip with composite ribs, an equivalent mass per unit length and section moment of inertia, based on the actual properties of the silicon strip with composite ribs, are used to calculate a single material density and strip thickness. This greatly reduces the number of elements and nodes, and therefore, the number of equations in the problem solution, and still produces very reliable results.

Boundary conditions applied to the model simulate the degrees of restraint provided by the 2-2-2 kinematic mount described in Section XX.XX of this report. In practice, three of these mounts are located at points equally spaced around both ends of the silicon shell structure. At one end, each mount prevents movement in the azimuthal and axial directions, but allows radial movement as well as several rotations. Mounts at the opposite end prevent only the azimuthal movement of the shell. Therefore, the silicon structure can expand and contract both axially and radially as needed. Cantilever mounting of the silicon shell is simulated by simply removing the latter restraints. Displacements due to gravity alone were calculated for both support configurations.

3.2.4.2 Thermal Distortion

To evaluate the effects of symmetric and asymmetric temperature distributions on the shape of the silicon shell a number of cases were considered. Results of these cases are summarized in Table 0-2. Cases 1A through 1D show that, as the temperature of the entire outer layer of silicon is varied from 2 to 8°C above the temperature of the rest of the structure, the resulting radial and axial expansions are fairly modest, even in the worst case. It should be noted also that these displacements are linear functions of temperature. Figure 0-18 shows the distorted shape of the shell when this kind of temperature distribution exists.

Figure 0-18. Deformed silicon shell.

In Case 2, a uniformly increasing temperature distribution is applied to one 120° arc segment of the outer layer of strips between kinematic mounting points. The temperature difference ranges from 1°C, for the strips at each end of the arc segment, to 8°C for the two strips at the center of the segment. In this case it is noted that the maximum radial displacements do not differ significantly from those in Case 1C and 1D. However, when the same temperature distribution is applied to the inner layer of strips as well, the maximum radial displacement nearly doubles,while the maximum axial displacement is about the same. Similar results are produced when the three

center strips in the same arc segment have temperatures of 4 and 8°C applied as in Cases 4 and 5. In Case 6, a uniformly increasing temperature distribution is applied over the length of the center strip in the outer layer of the same arc segment. Temperature differences range from 2°C at each end of the strip to 8°C at the strip center. Displacements in this case are still relatively small.

Table 0-2 Central Region Thermal Distortion

Case	Description	Max. Radial Displ. (μm)	Max. Axial Displ. (μm)
1A	Outer silicon layer at uniform temperature of 2°C	1.56	1.23
1B	Outer silicon layer at uniform temperature of 4°C	3.20	2.45
1C	Outer silicon layer at uniform temperature of 6°C	4.80	3.68
1D	Outer silicon layer at uniform temperature of 8°C	6.40	4.91
2	Outer silicon layer symmetric temperature distribution over 120° sector; temp. distribution 1-2-3-4-5-6-6-5-4-3-2-1°C	5.41	1.99
3	Same distribution as Case 2 over both inner and outer silicon layers	10.00	1.92
4	Outer silicon layer symmetric temperature distribution over center three strips of 120° sector; temp. distribution 4-8-4°C	4.90	2.21
5	Same distribution as Case 4 over both inner and outer silicon strips	9.03	2.19
6	Outer silicon strip symmetric temperature distribution over length; temperature distribution 2-4-6-8-6-4-2°C	2.49	0.94

While the results of the nine cases are not conclusive, they do suggest that temperature differentials ranging to 15°C, due to poor heat transfer from strips in a *single layer*, may not cause displacements that exceed the design tolerances. Reduced heat transfer in this instance may be caused by local separation of the wick from the cooling ring, partial separation of, or discontinuities in a silicon strip bond joint, nonuniform convection at the strip surface, or any combination of these. On the other hand, any of these conditions that cause poor heat removal from both layers of silicon in the same region may result in unacceptable radial displacements.

3.2.4.3 Gravity Effects Maximum displacements due to self weight of the shell were calculated for two kinematic constraint conditions. In the first case, the shell is assumed to be supported at both ends with the boundary conditions simulating the restraints described above in Section II, Model Description. Under these conditions the maximum sag due to gravity occurs at midspan of the top-most and lower-most sets of strips, as expected. The magnitude of these displacements is about 12.2 μm. If this displacement is superposed on the worst case radial displacement due to thermal distortion (Case 3, Table XX.XX) the total maximum radial displacement of some of the lower-most strips could exceed 20 μm. It should be noted that, in this model, the unsupported length of silicon is 224 mm. In a recent design revision the unsupported length was reduced to only 170 mm by moving the cooling rings closer together. Since the lateral stiffness of the silicon is a function of the cube of its length the maximum sag due to gravity may be only 5–6 μm. The shorter unsupported length will also reduce the radial displacement due to thermal loading. Thus, some improvement in overall stiffness of the structure can be expected if the latest design revision is implemented. This revision will be reflected in the next generation finite element model.

Gravity sag distortion of a shell supported in a cantilever manner was also considered. In this case boundary conditions simulating a modified 2-2-2 mount capable of reacting certain moments were applied. As in the first case, the maximum displacements occur at midspan of the upper and lower sets of strips, but with an additional out-of-plane bowing of both cooling rings. While the bowing for this diameter shell is only a few microns, it is expected that it would be much more pronounced for the larger shells because of the increased span between support points. This, in turn, would contribute to increased midspan sag. The sag for this particular model is still only 14.5 μm. Even so, cantilever mounting is probably not a viable alternative because the geometry is extremely sensitive to external forces applied to the free end of the shell. Such forces could be caused by the large number of electrical jumpers connecting the shell to a distribution bus.

3.2.4.4 Natural Frequency

The fundamental frequency was calculated for a silicon structure supported by mounts on both ends as described in section II. Under these conditions the first frequency is about 165 hz. This relatively high frequency can probably be attributed to the high stiffness of the mounting. The next generation shell model will include boundary conditions that simulate the tangent bar mount described in Section XX.XX of this report. It is possible that , because these devices may have greater compliance than the 2-2-2 mount, the shell structure could experience a rigid body motion with a somewhat lower frequency.

3.2.5 Silicon Module Detector Assembly Prototype detector modules for the tracker's central and forward regions will be constructed with an automated, computer controlled assembly and alignment system. The primary objective of this activity is to demonstrate the feasibility of constructing bonded silicon structures that meet the most stringent tolerance requirement of 5 μm. The integrated system includes a manipulator (pick-and-place machine) for handling individual silicon strips, a feed device for preparing individual strips for the manipulator, a rotary alignment fixture for supporting, indexing, and aligning the cooling rings, adhesive dispensers, an optical alignment system, and a controller. This section describes the design and operation of the mechanical and control sytems. The optical alignment system is discussed in Section XX.XX of this report.

3.2.5.1 Requirements To produce a large number of very precise silicon modules, each constructed with numerous bond joints of consistent high quality, the assembly process is automated to the greatest extent practical. The basis for the assembly system design is the silicon module's most stringent fabrication tolerance. In the central region, for example, the silicon strips comprising each module must be placed within 80 μm in the radial (R) direction, within 250 μm in the axial (Z) direction, and within 5 μm in the azimuthal (ϕ) direction. While it is possible to satisfy the first two requirements using conventional methods, more sophisticated techniques in material handling, inspection, and alignment are needed to meet the third requirement. Commercial equipment incorporated in the assembly system overall design is selected on the basis of stability and precision. Unique or custom designs used throughout the overall design are based on established techniques and principles of precision mechanics and optomechnical design.

A primary goal in the development of this system is a design that satisfies the operational requirements for the construction of both central region shells and forward region planar arrays. The design described in this section achieves that goal. In this design, all the equipment is mounted on a large optical table, and the rotary fixture, which is the component most difficult to set up and align, remains fixed for construction of either type of structure. The other pieces of equipment are modular and can easily be repositioned and realigned when changing from one structure type to another. Figures 0-19 and 0-20 show the equipment arrangements needed to construct both types of silicon structures.

In the following discussion, emphasis is placed on the construction of the central region silicon shells because they are the most difficult to fabricate. Although some minor variations in mechanical equipment design are necessary because of the shapes and sizes of the silicon strips, the basic construction operations are generally the same for both types of structures. The following sequence of operations outlines the construction of a typical silicon module:

Figure 0-19. Central region silicon shell assembly arrangement.

Figure 0-20. Forward region silicon array assembly arrangement.

1. manually mount and align pair of cooling rings on rotary fixture,

2. apply adhesive to silicon strip mounting surfaces on cooling rings,

3. index, inspect, and realign rotary fixture,

4. manually place silicon strip in manipulator feed device,

5. verify silicon strip's orientation w.r.t. manipulator end effector

6. retrieve silicon strip from the feed device with manipulator,

7. apply adhesive activator to silicon strip,

8. position silicon strip near mounting surfaces on cooling rings,

9. inspect, realign silicon strip with manipulator end effector,

10. place silicon strip on cooling rings

11. place kinematic mount components, and

12. remove finished silicon structure.

3.2.5.2 Mechanical System Description The design, operation, and salient features of the major mechanical subassemblies comprising the silicon module assembly system are discussed in this section. Most of these subassemblies are identified in Figures 0-19 and 0-20. Components of the optical alignment system have been omitted for clarity. Figures showing the relationship between the optical alignment system and the mechanical assembly system can be found in Section XX.XX of this report.

3.2.5.2.1 Manipulator The manipulator is used primarily for the transfer of individual strips from the feed device to the cooling rings on the rotary fixture. Its base unit has three translation stages and one rotary stage. Two of the translation stages are horizontal and the third is vertical, with all three stages being orthogonal to one another. Each translation stage is ball screw-driven with a d.c. servo motor and includes a glass linear incremental encoder for position indication. The encoder has a line grating of 50 lines per millimeter and, when used with 128X logic, provides a resolution of 0.156 μm. Although there is no speed requirement for this application, the linear system is capable of this resolution at speeds ranging to 0.50 m/second. A fail-safe electromechanical brake is included on the vertical translation stage to prevent drift when the motor is deenergized. The rotary stage, which is carried by the vertical translation stage, carries the manipulator arm with its end effector. This stage is a geared, d.c. servo-driven unit with a glass rotary encoder for position indication. The encoder has a resolution of 50,000 counts per revolution, or an accuracy of $\pm$25.9 arc seconds, when 20X logic is used for position control.

Before a silicon strip is placed on the cooling rings, its orientation must be varified by viewing its alignment fiducials with a pair telescopes, which are part of the optical alignment system. If correctons are needed, they are made with the manipulator's end effector. This device, shown in Figure 0-21, is a vacuum platen mounted on three piezo-driven rotary stages. The rotary stages provide the necessary roll, pitch, and yaw motions for final alignment of the silicon strip immediately before it is placed on the cooling rings. Flexures, rather than ordinary radial bearings, are used for the rotary stage pivots because they provide smooth, frictionless motion without backlash. The piezoelectric translator driving each stage can produce a maximum angular displacement of about 8.0 milliradians. This angular displacement results in linear displacements in the range of 200 to 400 μm, at the location of the alignment fiducials near the ends of the silicon strip. Because of the space constraints imposed by the different equipment configurations, the end effector can be mounted in any attitude with the vacuum platen in either of two orientations relative to the rotary stage subassembly. For example, when placing silicon strips on the inside of the

cooling rings during the construction of a central region shell, both the rotary stage subassembly and the vacuum platen must be in the horizontal attitude to fit inside the rotary fixture. When placing silicon strips on the outside of a shell, or on either side of a forward region array, the rotary stage subassembly must be in the vertical attitude with the vacuum platen in the horizontal orientation. This configuration is necessary because the space between the the rotary fixture and the alignment telescope is limited by the telescope's focal length. Other access limitations make it necessary to use several interchangable manipulator arms for the construction of the different silicon structures.

Figure 0-21. Manipulator end effector.

3.2.5.2.2 Silicon Strip Feed Individual silicon strips are prepared for transfer to the manipulator by a manually loaded feed device. For the manipulator to receive the strip in the proper orientation, that is, within the range of motion of the end effector, the strip must first be accurately positioned. After a strip is placed on a vacuum platen in the feed mechanism, it is transferred to a location under an inspection device to determine its orientation. If alignment is needed, the vacuum platen

is repositioned by a set of piezoelectric translators; then, it is returned to its initial loading position where the silicon strip can be picked up by the manipulator. While this strip is being placed on the cooling rings by the manipulator, the loading and alignment process can be repeated with a new strip. The piezo translators for the vacuum platen are arranged to produce both linear and rotary alignment motions. The vacuum platen and piezo translators are mounted on a translation stage similar to the ones used for the manipulator base unit. Several position inspection devices for determining the orientation of the strip in the feed device are being considered for this application.

3.2.5.2.3 Rotary Fixture The rotary fixture serves not only as a mount for cooling rings and structural rings for both types of silicon structures, it also performs the incremental indexing function during construction of these components, and it provides a means of actively compensating for runout errors. Three major subassemblies comprise the rotary fixture; they include a spindle, an alignment platform, and a rotary bearing set. The relationship of these subassemblies is shown in Figure 0-19.

A rotary bearing set, composed of a pair of precision single-circle goniometers, supports the spindle assembly and alignment platform. The primary bearing in the set is a large goniometer with a 400 mm diameter bore. This bore is the manipulator access to the inside surfaces of a pair cooling rings for a central region shell mounted on the spindle. One of the two stages of the alignment platform is mounted on the rotating ring of this goniometer, and the second stage is attached to the large open end of the spindle. The other end of the spindle is supported by a much smaller goniometer. A d.c. servo motor drives the rotating ring of the large goniometer, alignment platform, and spindle as a unit. Angular position of the entire assembly is indicated by the output from a glass incremental rotary encoder. The small goniometer is mounted on a set of XYZ translation stages, similar to those used for the manipulator base unit, so that lateral (X) and vertical (Y) adjustments can be made during the initial alignment of the system. The Z, or axial stage has a much longer stroke, and is used to remove a silicon structure from the spindle when it is finished. This procedure is described in item (6).

The small goniometer has an 80 mm diameter bore for on-axis mounting of a small sphere used for establishing the optical reference axis for the spindle alignment system (Section XX.XX). Another sphere, which is also a part of this alignment system, is mounted on the second stage of the alignment platform at the open end of the spindle. While a silicon strip is being placed on the inside of the cooling rings, this sphere, which is mounted on a short lever arm, is stored between the alignment platform stages outside the bore of the spindle. After the strip has been placed, and the spindle indexed, its alignment is checked by pivoting the sphere into position at the center of the spindle bore and observing the resulting fringe pattern from the reference laser

beam. Realignment is done with the alignment platform described in the next paragraph. To ensure that the sphere insertion into the bore is repeatable with a high degree of accuracy, the lever arm to which it is mounted, is pulled into a kinematic mount by a linear spring motor. The lever arm is pivoted back to its storage position by a small power screw driven by a miniature d.c. servo motor. Since the precise location of the sphere in the bore of the spindle is determined by the kinematic mount alone, the rest of the mechanism can be fairly imprecise.

Radial deviation of the small goniometer is predicted to be less than 5 μm, but that of the large one may be as much as 10 μm. To permit active realignment of the spindle's axis, the end of the spindle supported by the small goniometer is coupled to the goniometer's rotating ring with a flexure pivot universal joint. This allows the spindle's axis to be pivoted slightly about the universal joint's two orthogonal axes by moving the opposite end of the spindle. The two-stage alignment platform mounted on the large goniometer's rotating ring serves this purpose. Geometrically, the platform is a short, truncated pyramid structure with its stages mounted in tandem, i.e., one stage carried by the other, and coupled by links with flexure pivots. The stages move orthogonally in much the same way as a set of conventional XY stages. The links connecting one stage to another lie in two planes that form oppposite faces of the pyramid, with their virtual line of intersection on one axis of the spindle's universal joint. Thus, when a lateral force is applied to a stage, its motion is very nearly linear for small angular displacements of the links. In this application, the lateral displacements are approximately $\pm$1.00 millimeters. The motive force is applied to a stage through a mechanism that provides a mechanical advantage of more than 15 to 1. The actuator for this motion is a commercial, long stroke piezoelectric translator. Although this device has a load capacity of only 1.5 Kg when used alone, it is capable of moving a 23 Kg payload in this instance because of the mechanical advantage. This is important because the actuator must be capable of reacting gravity loads of mechanical components in the platform/spindle assembly. Resolution of the translator, which is expected to be about 4 nanometers, is more than adequate for this application. Overall compliance of the mechanism is estimated to be less than 5 μm for a design payload of 16 Kg. Because flexures, rather than conventional radial bearings, are used throughout the spindle and alignment platform assembly, the entire mechanism is frictionless and free of backlash.

The backbone of the spindle is a cylindrical shell with a number of axially oriented oblong slots through its wall. Since the spindle must have some structural continuity over its length in order to support a silicon shell, and at the same time provide access for placement of silicon strips on the cooling rings' inner diameters, a cage-like structure is needed. Even though the number of longitudinal webs in this structure is minimized, some of the internal silicon strips can not be placed because the surfaces to which they are to be attached are obscured by the webs. After strips have been placed on all the accessible inner surfaces on the cooling rings,

the partially completed silicon shell must be rotated, relative to the spindle shell, to expose the unused surfaces. This concept is implemented by mounting a narrow rotary table on a set of large bore bearings at each end of the spindle. These tables carry backing rings to which the individual cooling rings are mounted. The rotary tables are initially locked to the spindle shell while all the accessible surfaces are covered with silicon strips, then unlocked so the partially completed shell can be indexed to expose the remaining surfaces. Two spindle shell sizes are needed to construct all four central region shells because the smallest shell's inside diameter is not large enough to accept the manipulator arm needed for constructing the larger silicon shells.

Before construction of a central region shell can begin, the individual cooling rings must be mounted on rigid backing rings to facilitate handling and alignment on the spindle shell. A set of studs, bonded to a cooling ring wall, are clamped by small fixtures attached to the backing ring. After the cooling rings are clamped in place, the backing rings are mounted on the spindle shell's rotary tables. The cooling ring is centered on the spindle by manipulating the backing ring with three micrometer heads attached to the rotary table. These are removed after this alignment is finished. Azimuthal, or "clocking" alignment of the cooling rings is done with the rotary tables.

3.2.5.2.4 Adhesive Dispenser To date, only preconceptual design work has been done on the adhesive dispensing problem. It is apparent, however, that a method of applying a high viscosity adhesive to the cooling ring surfaces, or to the silicon strips, in precisely controlled amounts, is required. A single part system, rather than a two part system with adhesive and activator, is the most desirable for this application because the adhesive would have to be applied only to the silicon strip immediately before it is placed on the cooling rings. In contrast, a two part system requires that the adhesive be applied to the cooling ring surfaces, a process that further complicates the assembly procedure because additional application equipment with more complex software is needed. If a two part system is necessary, it would be advantageous to use the manipulator with an adhesive dispensing head in place of the vacuum platen end effector for applying the adhesive to the cooling ring surfaces.

3.2.5.2.5 Placement of Kinematic Mount Features Only preconceptual work has been done on the placement of kinematic features. If the kinematic mount on the graphite composite shell is an adjustable tangent bar, as described in Section XX.XX of this report, the feature on the silicon shell structure can be a simple hemisphere bonded to the beryllium layer on the silicon strip. Since the tangent bar is adjustable, the placement tolerances can be relatively liberal, and the

six hemispheres can be placed manually with simple fixtures and micrometer heads temporarily mounted on the spindle shell's rotary tables.

3.2.5.2.6 Silicon Structure Removal Before a completed silicon structure can be removed from the rotary fixture, it must first be stabilized to prevent rotation about its axis. A spider ring, rigidly fixed to the small goniometer base, is coupled to the backing ring to which the nearest cooling ring is mounted. The cooling ring at the opposite end of the silicon structure is then released from its backing ring by releasing the stud clamping fixtures. Several fasteners, which join the small goniometer and the nearest backing ring to the spindle shell, are removed. At this point in the removal process, the silicon structure, still attached to one backing ring, is supported by the spider ring in a cantilever manner. The entire assembly can then be transferred in the axial direction, by the small goniometer's Z translation stage, until it clears the spindle shell. In the fully retracted position the silicon structure can be manually removed from the backing ring.

3.2.5.3 Control System Description The control system for the silicon module detector assembly system is a PC based controller with capabilities to control 16 axes of servo motors, two axes of long stroke piezoelectric translators, and three axes of short stroke piezoelectric translators. Several axes are under closed-loop control with closed-circuit TV cameras, position sensitive devices (PSD), fiber optic probes, and laser interferometers acting as the position sensors. The system also controls the vacuum service for the platens on the manipulator end effector and silicon strip feed device, as well as the pneumatic service for the adhesive dispenser. Diagnostic data is transmitted to a microcomputer that serves as a data logging, graphing, archiving, and trending device using commercial software. Figure 0-22—is a block diagram of the control system.

3.2.5.3.1 Actuator Controllers Control for all 16 servo motor axes is over one RS232C interface channel. The commercial controllers are capable of interpolation of encoder data to obtain resolutions of 0.156 μm. Velocity and acceleration profiling is also possible. The discrete input/output capability of the controller is used for limit switch inputs and electronic fail-safe brake control on some of the axes.

All three axes of the short stroke piezoelectric actuators on the manipulator end effector receive motion commands, via one RS232C interface channel, from a commercial controller. Similarly, the two long stroke piezoelectric actuators for the alignment platform's axes are controlled

Figure 0-22. Control system block diagram.

by another commercial controller, over a single RS232C interface channel. All five piezo-driven axes are under closed-loop control.

3.2.5.3.2 Sensors At least two channels of video, using a commercial frame capture board located on the PC backplane, are used as position feedback. A computer controlled video multiplexer is located in an adjacent slot on the PC backplane so that multiple channels of video require only one frame capture board. Sub-micron position information is extracted from the video using centroid finding algorithms. This type of position sensing is particularly useful for positioning based on distinctive features of an object, such as the corners of the silicon strip, or the fiducials on the strip.

Position sensitive devices (PSD) are similar to quad cells in that they develop a voltage that is proportional to the position of a laser beam impinging on its surface. The major disadvantage of the quad cell is that the beam must cover a portion of all four quadrants to produce accurate results. In contrast, the PSD has no such requirement, so the beam can be located anywhere on its surface and does not have to be close to the center of the device. The only requirement is that the beam strike the surface of the PSD. Another advantage of the PSD is that it is capable of

sub-micron resolution. Output from the PSD is amplified and processed with an electronic analog processor, and the result read by the PC controller through a 16 bit A/D converter located on the backplane of the computer.

The fiber optic probe is a new technology applied to the measurement of displacements in the sub-micron range. Output voltage of the device is proportional to the distance between the surface of an object and the tip of the probe. The voltage is read by the PC controller through a 16 bit A/D converter located on the backplane of the computer.

Long term stability of the assembly system is measured with a laser interferometer capable of measuring distances with sub-micron resolution. Three channels of the interferometer are read by the PC controller over a single RS232C interface channel.

3.2.5.3.3 Software Software for the controller is a DOS based program written in the 'C' language with a graphical human interface. A control library for each of the devices served by the PC is written in such a manner that the actual machine control algorithm can be understood by programmers unfamiliar with the 'C' language. The controller is also capable of individual control and data logging from each device.

The data logger is connected to the PC controller through an RS232 channel, or through a dedicated PC interface line. The computer can display plots of real time data or recall previous data that has been recorded to disk. Data logger operation is independent of the PC controller.

3.3 MATERIALS SELECTION AND TESTING

3.2.5.3 Materials Considerations

3.2.5.3 Materials Testing The materials testing program first pursued mechanical performance information on the advanced-composite-materials system of interest. This was done to ensure that mechanical properties necessary for STS alignment and stability were offered by these materials. The need to define and quantify higher order stability effects, such as hygrothermal, would have been obviated if the mechanical constraints of the STS design had not been fulfilled. The elastic properties of the chosen materials system are of greatest importance to STS performance. Because positional and dimensional stability are paramount, the support structures' performance

will be strain-limited and hence experience a very low state of stress. The inelastic behavior of the materials is consequently of much lesser importance. The need for micron-level stability, as stated in the design requirements of Table XX, defines this situation. These requirements indicate the need for a stiff structure with minimized passive and dynamic instabilities. Passive characteristics such as dimensional stability and dynamic attributes such as the response to vibrational excitations are both positively influenced by the use of high elastic modulus structural materials. The inherent stiffness of a structure depends on the moments of inertia and elastic moduli of its members. The STS, which must be supported stably using as little mass as possible inside a small volume, will have to maximize the use of stiff materials because the thin-walled sections of its members have small moments of inertia. Therefore, the high modulus materials will enhance system stability by minimizing gravity induced deflections and stresses, which will further minimize the prospect of creep instability. The dynamic performance of the system improves as a function of increased stiffness because its natural vibrational modes are shifted to higher frequencies where the vibratory inputs have lower amplitudes and are hence, less deliterious to positional stability.

Parallel mechanical test programs were performed at LANL and Programmed Composites, Inc. (PCI) of Brea, California. Sandia National Laboratories Albuquerque, (SNL) also evaluated the elastic moduli of a number of samples. This parallel testing program was designed to promote confidence and enhance quality assurance. All specimens were fabricated by PCI who subsequently tested 10 of each type and forwarded 5 specimens to LANL. Table 0-3 demonstrates the scope of the mechanical testing program.

Table 0-3 P-75S/954-3 Mechanical Properties Test Matrix			
Test	Neat Resin	Uniaxial	QI
0° Tensile Strength, Modulus, and Poisson Ratio	X	X	X
0° Compressive Strength and Modulus	X	X	X
In-Plane Shear Modulus. and Strength	X	X	—
Interlaminar Shear Modulus and Strength	—	X	—
90° Tensile Modulus and Poisson Ratio	X	X	X
90° Compressive Modulus and Strength	X	X	X

3.3.2.1 Specimen Fabrication PCI fabricated a full complement of neat resin, longitudinal-, transverse-, and quasi-isotropic- (QI) fiber specimens for mechanical testing. Fiberite, Inc. 954-3 cyanate ester resin was used for all specimens, while Amoco P-75S high-modulus graphite fiber was used in the fiber-bearing specimens. Properties of P-75S are presented in Table 0-4.

The characteristics of interest for this resin system are intermediate to high mechanical properties, low moisture absorption, and very low micro-cracking. These are ideal for use in low mass, dimensionally stable structures. The resin processes similar to epoxy systems used for structural composites, including a 177°C autoclave cure cycle. The pure cyanate resins exhibit low tack and also have a low minimum viscosity during cure that is below 100 centipoise. The low viscosity reached during the cure makes a laminate more susceptible to variation in fiber volume because resin bleed is more difficult to control accurately and consistently. Another factor requiring control is the resins' hygroscopic behavior in the uncured state. Neat resins and prepregs with cyanate ester must be prevented from extended exposure to high humidity to prevent voids in a laminate or neat resin casting caused by water vapor formed during cure. The resin or prepreg requires sealing in airtight bags at all times when not in use. Standard methods for packaging as used for epoxy/fiber prepregs are adequate if adhered to closely.

Table 0-4 Typical P-75S 2K Graphite Fiber Properties and Characteristics[a]	
Tensile Strength	1.9 GPa
Tensile Modulus	520 GPa
Density	2.0 Mg/m^3
Filament Diameter	10 μm
Elongation at Break	0.4%
Elastic Recovery	100%
Carbon Assay	99 +%
Surface Area	0.35 m^2/g
Longitudinal Thermal Conductivity	185 W/mK
Electrical Resistivity	7 mohm-m
Longitudinal CTE at 21°C	–1.35 ppm/K

[a]Amoco Performance Products, Inc., Product Sheet F-5817, Rev. 4., "THORNEL Carbon Fiber P-75S 2K," 1320 Willow Pass Road, Ste. 401, Concord, California 94520

Even though the resin cure cycle is very much like that of an epoxy resin, considerable effort was expended to develop a cure cycle and bleeding scheme that produced consistent, acceptable fiber volume results. Target fiber volume was 60% to 65%. The cure cycle stipulates when the pressure is applied to the laminate and at what viscosity or state of gelation. The bleeding scheme is the type and number of plys used to absorb resin from the laminate to control fiber volume. The bleeder plys used were glass fabrics (styles 112, 120, 181, and 220 in various combinations) which have a greater degree of consistency than nonwoven bleeder materials.

A total of four autoclave cures were made to determine a cure cycle and bleeding scheme that produced acceptable fiber volumes. The first test was aimed at verifying Fiberite's recommended cure cycle, C-9, and used a bleeding scheme that would be appropriate for most resins such as epoxies. The cure requires temperature hold at 121°C for one hour with the pressure being applied 15 minutes into the hold. After the hour at 121°C is completed, the temperature is increased to 177°C for a two-hour hold. This cure cycle produced fiber volumes up to 69% which may cause a significant degration in interfacial properties of the laminate. A matrix of laminates was then fabricated on subsequent autoclave runs using various bleed layers and daming

techniques for controlling resin flow. PCI's Signature Process Control was used during several of these runs which characterized the capacitance response of the resin during cure. Based on the information collected, the C-9 cure cycle was modified to delay pressurizing the autoclave until after full staging at 121°C and the temperature has reached 149°C. The Signature Process Control monitoring also demonstrated that cross-linking of the polymer was generally complete after one hour at 177°C, the additional hour not contributing significantly to the cross-linking of the resin matrix but serving to ensure complete cross-linking throughout the laminate.

Percent fiber volume and void content were measured on all laminates and void content measured on the neat resin castings. Fiber volume and voids were measured using the acid digestion method per ASTM-D-3171. The results of these tests are shown in Table 0-5.

Table 0-5 Acid Digestion Results Per ASTM-D-3171

Laminate	Average Fiber Volume (%)	Average Void Volume (%)
8-Ply QI	62.2	+0.02
8-Ply Uni	60.3	−0.95
20-Ply QI	58.5	−0.37
20-Ply Uni	58.7	−0.77
160-Ply Uni	55.6	+0.77
Neat Resin	—	+1.68

Sources of error which account for negative calculated void content are theoretical fiber densities and loss of fiber during filtering of the fibers. High-modulus fibers are particularly sensitive to fiber loss during the filtering process. Negative calculated voids are indicative of a very low fiber volume and not a process error or significant measurement error. Void content measurements that are negative should be assumed to be zero within the accuracy of the test procedure.

The tensile coupons used for the composite specimens were per ASTM-D-3039 and cut 12.7 mm × 228.6 mm with 31.8 mm-long G-10 tabs with tapers. The neat resin test specimens were dogbones per ASTM-D-638 cut 114.3 mm long × 12.7 mm wide. The 20-ply compression test specimens for the Wyoming Modified Celanese method were 114.3 mm long × 12.7 mm wide. G-10 tabs 31.8 mm long with no tapers were used.

3.3.2.2 Testing Systems and Fixtures

LANL used a Materials Testing Systems, Inc. 880 hydraulic device while PCI used a SATEC SYSTEMS 50 UD hydraulic loading machine. All test specimen fabrication and testing

was performed using applicable ASTM standards listed in Table 0-6. The specimen grips used for the tensile loading were manufactured by MTS, #649, and are of a side-loading and mechanical wedge design. The individual test fixtures used for the program included the Celanese compression test fixture, which was first introduced by the Celanese Corporation in 1971 and was later accepted by ASTM as ASTM-D-3410 in 1975. The two halves of each cone-shaped wedge grip, which are provided with alignment pins both between themselves and with the other wedge grip, are bolted together after the specimen is inserted between them, using the spacer bar provided to establish the distance between grips. Overall alignment of the fixture halves is also aided by a close-fitting sleeve that slides over the assembly after the specimen is installed and the spacer bar removed. It is frequently criticized, however, because of its cone-in-cone arrangement of the wedge grips. In order to maintain full surface contact between each pair of split half-cones and the mating conical cavities in the end blocks, the tabbed ends of the specimen must be fabricated to a precise thickness. Otherwise, the split-cones will not be circular when assembled.

Table 0-6 American Society of Testing and Materials Standards

Test	ASTM Designation
Acid digestion composition determination	ASTM-D-3171
Tensile test	ASTM-D-3039-76
Celanese compression test	ASTM-D-3410
Iosipescu shear test	approval pending
Other applicable standards	
Compressive properties of unidirectional or crossply fiber-resin composites	ASTM-D-3410-87

The Wyoming Modified Celanese fixture was used for all compressive loading tests and is designed for a nominal specimen thickness in the tab regions of 4.2 mm. With the grips protruding up to 6.4 mm, a tabbed specimen up to that dimension can be accommodated.

The standard gage length, distance between tabs, for all compression test fixture configurations following the general guidelines of ASTM Standard D 3410 is 12.7 mm. Thus, the tab length for standard specimens used with the Wyoming Modified Celanese Compression Test Fixture is 50.8 mm. All parts other than the cone-shaped wedge grips, alignment pins, and fasteners are made of 1018 cold rolled steel, black oxide treated to reduce rusting and corrosion when kept lightly oiled. The serrated wedge grips are A6 tool steel, heat treated to R_c55, to provide durable gripping surfaces.

The Iosipescu shear test fixture was actively developed for use with composite materials during the early 1980s. An ASTM standard has been written and is pending approval. The standard test specimen is 76.2 mm long, 19 mm wide, and of any thickness up to 12.7 mm. Typically, a specimen approximately 2.5 mm thick is used. A 90° notch is machined into each edge of the specimen, and a strain gage can be mounted to monitor shear strain.

3.3.2.3 Tests Results and Conclusions

The test methods used by LANL and PCI were similar, conventional load frame-and load cell-based. SNL, however, used nondestructive methods, scanning electron microscopy (SEM) and scanning acoustic microscopy (SAM), to determine the elastic properties of specimens. The data generated by all institutions and methods were comparable and contributed to confidence in the findings.

The neat resin test results were the most uniform among the testing institutions as demonstrated by Table 0-7. This is reasonable because fewer processing steps are required and fibers are not introduced, both of which instill variability in test results. Theoretically, there is no difference in the fixturing or execution of the tests for neat resin versus fiber-bearing samples, even though the lowest level of loading is sustained by neat resin. The elastic tensile, compressive, and shear moduli are smaller than the highly cross-linked epoxy resins such as 3501-6 and 934. The cyanate ester chosen has comparable elastic performance and much superior moisture absorption and micro-cracking characteristics however. This situation is acceptable because the structural components will primarily derive their stiffness from the high elastic modulus reinforcing P-75 fiber. Also, the moisture-induced dimensional instability, which is dominated by the resin, will be diminished by the choice of this materials system.

The post butane and 10 Mrad irradiation exposure test results for the neat resin are very encouraging. The minimal perhaps even statistically insignificant, decrease in the elastic mechanical performance indicates that little fabrication stress relief is occurring in the resin due to those conditions. The absence of dense cross-linking is responsible for this effect in the cyanate ester resin.

The comparison of LANL's test program results with that of other published data can be seen in Table 0-8. As previously mentioned, the scarsity of data on cyanate ester resin systems led to the choice of the seminal C.C. Chamis data for highly cross-linked polymeric neat resins as a means for comparison. Also, the recently published data for 954-3 cyanate neat and fiber-bearing resin by its manufacturer, fiberite, Inc., are used for comparison. As demonstrated by the Table, 954-3 is comparable to an intermediate modulus, high strength (IMHS) hygroscopic resin according to Chamis. The differential in strength is more exaggerated as well as confusing. The

Table 0-7 Mechanical Properties Test Results for P-75S/954-3 Laminates Normalized to 60% Fiber Volume Fraction

Mechanical Property	Test Institution	Specimen Description			
		Neat	0°	90°	QI
Elastic Tensile Modulus (GPa)	LANL	3.7	323	6.9	100
	LANL*	3.4	321	6.6	110
	PCI	3.8	324	6.4	96.5
	SNL	3.7	280	8.1	97.5
	[Average]	3.7	309	7.1	98
Elastic Comp. Modulus (GPa)	LANL	3.7	300	6.7	81.3
	LANL*	3.5	283	6.8	81.3
	PCI	3.4	270	6.2	77.2
	[Average]	3.6	285	6.5	79.0
Elastic Shear Modulus (GPa)	LANL	1.2	4.5	1.7	—
	LANL*	1.1	4.8	1.7	—
	PCI	1.2	4.0	1.6	—
	SNL	1.4	4.4	2.6	—
	[Average]	1.3	4.3	2.0	—
Poisson's Ratio	LANL	0.38	0.25	0.0043	0.28
	LANL*	0.37	0.25	0.0031	0.31
	PCI	0.40	0.32	0.0063	0.33
	SNL	0.40	0.32	0.0060	0.33
	[Average]	0.39	0.3	0.0055	0.31
Ultimate Tensile Strength (MPa)	PCI	60	1000	23.4	294
Ultimate Comp. Strength (MPa)	PCI	—	337	41.7	131
Ultimate Shear Strength (MPa)	PCI	27.1	39.2	19.4	—

*Denotes radiation, 10 Mrad, and butane environmentally conditioned specimen results which are not included in the average computation.

954-3 test results demonstrate a 44% lower shear strength than the IMHS while 954-3 possesses a 24% higher tensile strength. The manufactures' estimate of the resins' tensile strength differs

by only 6% from that of the LANL test program. This discrepency in conjunction with the absence of the manufacturers' data for ultimate shear strength renders the LANL shear strength data questionable. It is note worthy that only one institution performed inelastic property tests for the program, hence their results have not been corraborated. Of greatest importance, however, is the fact that the elastic properties of the 954-3 resin are well defined and in agreement with the manufactures published data where available. This is true because of the aforementioned strain-limited performance of the STS hardware and the fact that the IMHS resin system of Chamis is a highly cross-linked system and not a cyanate ester.

Table 0-8 Comparison of Mechanical Properties Test Results with Published Mechanical Properties

	LANL Average		Chamis Data[a]	Fiberite Data[b]	
Test	Neat Resin	Laminate 0° Uni.	Neat Resin	Neat Resin	Laminate 0° Uni.
Elastic Tensile Modulus (GPa)	3.7	309	3.4	2.76	296
Elastic Compressive Modulus (GPa)	3.6	285	—	—	241
Elastic Shear Modulus (GPa)	1.3	4.3	—	—	—
Poisson Ratio	0.39	0.3	0.41	—	—
Ultimate Tensile Strength (MPa)	60	1000	48.2	56.5	1000
Ultimate Compressive Strength (MPa)	—	337	145	—	359
Ultimate Shear Strength (MPa)	27.1	39.2	48.2	—	58.6

[a]C. C. Chamis, "Simplified Composite Micromechanics Equations for Hygral, Thermal, and Mechanical Properties," *SAMPE Quarterly*, April 1984, p. 17.

[b]ICI Fiberite, "ICI Fiberite Materials Handbook," 2055 East Technology Circle, Tempe, Arizona 85284, November 1, 1992, Rev. C.

The fiber-bearing specimen data is generally consistent, with the nondestructive testing methods demonstrating the largest departure from other findings. Again, the butane and 10 Mrad radiation exposure have a statistically insignificant effect on the mechanical performance of the laminates. The largest performance reduction is seen in the elastic shear modulus, differing by 15% after environmental conditioning. Closer inspection of this data reveals that the spread of the data from the three testing institutions is a maximum for this case. As noted, the nondestructive

method differs from the average of the destructive method by 21% whereas the conditioned sample differs from the destructive test average by only 3%. This places the accuracy of the nondestructive data in serious question for this attribute.

The lone laminate data for 954-3 is for a undirectional layup normalized to a 60% fiber volume fraction published in November, 1992 by Fiberite, Inc. The agreement of the LANL test program data with this is impressive for both the elastic and inelastic mechanical properties of the laminates, save the shear strength previously described.

The overall conclusion of the mechanical properties test program is that the P-75/954-3 materials system is now mechanically fully described and qualified. All elastic moduli and the poisson ratio of the system were evaluated by independent institutions using both destructive and nondestructive means to obtain comparable results. Inelastic parameters, though of lesser importance, were also defined, compared to published data, and found to be acceptable. The systems' sensitivity to a combination of liquid butane and 10 Mrad of irradiation was investigated and found to be negligible. A comparison to published data for an intermediate modulus, high strength densely cross-linked resin and to the manufactures' data for the neat and fiber-bearing resin proved to corroborate the results from the test program. This important agreement provided confidence in the materials systems' ability to meet the STS' performance objectives because the elastic properties of the materials system, as stated by the manufacturer in private communications and inferred from other technical sources, had provided the basis for STS performance calculations that proved acceptable. In summation, mechanical properties testing program has demonstrated the acceptability of the P-75/954-3 materials systems' mechanical performance for achieving STS baseline performance objectives.

3.4 COMPONENT ALIGNMENT AND STABILITY VERIFICATION Missing

3.5 EVAPORATIVE COOLING SYSTEM Missing

3.5.1 System Description Missing

3.5.2 Polystyrene Molded Wick Development Missing

3.5.3 Cooling Ring/Wick Development Tests Missing

3.4 Component Alignment and Stability Verification Status

3.4.1 *Silicon Subsystem Alignment* The assembly tolerance goals for the SDC silicon tracking system (STS) have been discussed in earlier reports, but they are listed here, in table 1, as a reminder of the extremely tight tolerances that must be met during assembly. In FY92 we produced engineering layouts for a precision machine to assemble STS barrel and planar array prototypes to meet the assembly goals; we defined and demonstrated the key alignment and assembly techniques for assembling high precision STS prototypes in FY93; we built and tested a prototype temperature controlled work space for assembly operations, and we developed a TV holography system to measure component and subsystem stability.

A method to align and glue silicon ladders onto cooling rings is needed to define the automated pick and place assembly procedure. Our alignment concept for assembling ladders onto cooling rings to make precision barrels for a STS, is shown in Fig. 1. From a stable reference line, two microscopes are positioned to view the exact location where alignment fiducials on silicon ladders are to be located as the ladders are glued to cooling rings during assembly. The key issues in implementing this alignment approach are defining: (1. a method to create a straight and stable reference line; (2. the technique for the precision placement and long term optical mechanical stability of the reference microscope assemblies; (3. defining how to sense the ladder fiducials and move the ladders, with precision, onto a reference system, and (4. gluing techniques.

Making a straight and stable reference line is not trivial, because even with the best commercial alignment telescopes, racking the telescope focus to mark a line of sight causes the line to wander more than the tolerances allowed for assembly. We were therefore forced to consider an alternate approach using 0.5 mw laser, a single mode fiber and a spherical ball. The single mode fiber acts as a distributed spatial filter to reduce laser beam wander to an acceptable level, and spherical aberration from the spherical ball lens marks the line of sight with a bulls-eye pattern without requiring any focusing adjustment. We have built the line of sight, and we are pleased with its operation, but we must still measure the long term stability of the line in a temperature controlled area and determine exactly how we will use the laser line for system set up.

In FY92, we demonstrated our alignment concept by positioning ladders, in a simulated alignment demonstration, to better than 1 μm. The demonstration, shown in Fig. 2, used a bar to simulate a ladder and a 20 μm pinhole to simulate a ladder fiducial. The pinhole position was sensed with a microscope and camera, and we used a computer to calculate centroid position for

a feed back control system. This configuration demonstrates all the concepts for our assembly alignment system. For a reference system monitoring, we attached a tooling ball to the center of the bar and monitored the ball position with an electronic autocollimator, which we converted into a long working distance microscope, with a lens. The lens, which attaches to the end of the electronic autocollimator barrel, and the tooling ball on the bar, change the angle measuring autocollimator into a stable position measuring instrument with 40 nanometer sensitivity. With this equipment we performed several tests. We randomly moved the simulated ladder away from the reference position, and then, using the closed loop feedback system with a centroid program to find the pinhole center, we repositioned the pinhole center back onto the reference position, which is the center of a crosshair in the microscope. This procedure demonstrated our ability to find the centroid of a small spot, and to use the information to reposition the spot onto a reference in a few seconds. With the electronic autocollimator we monitored the replacement accuracy for this alignment approach, and we verified that the ladders were always repositioned to better than 1 μm. We now have confidence that we can precisely position ladders to glue them onto cooling rings. We also measured the long term stability of the reference alignment hardware in an ordinary laboratory space where the room temperature changed by several degrees. Typically, we observed unacceptable mechanical drifts, of about 5 μm, during several hours of measurements. We attributed the drift to thermal expansion. These tests demonstrated the need for large, but inexpensive, controlled temperature assembly spaces (0.1°F) to assemble the STS.

Large commercial temperature controlled spaces are very expensive, so we built a prototype controlled temperature space using plastic walls, a plenum and a feedback system that regulated the brightness of a bank of light bulbs to control the temperature flowing past them into the plenum. A sketch of the design, which has been used at Livermore Laboratories to control the temperature around precision diamond point turning machines, is shown in Fig. 3. In our prototype room, the fans pushed about 2 work space air exchanges per minute past the light bulbs, through the plenum and into the work space. The controller maintained the working area temperature to better than 0.1°F, with air temperature outside room changing by roughly 5 degrees and with people walking in and out of the working area. Based on this prototype, we have decided to built similar temperature controlled work spaces over all our assembly areas. Inside the prototype temperature controlled work space area, we rebuilt the alignment reference equipment described in a previous paragraph, and we again measured the mechanical stability of the reference alignment equipment in the improved temperature environment. The results are shown in Fig. 4. Inside the temperature controlled room, the reference alignment system is stable to better than 0.5 μm over a 3 day test period. This is very encouraging. The experiment demonstrates the long term stability needed for the reference alignment system during assembly operations. We will continue to use this space to check and perfect the stability of our reference systems and incoming hardware as we prepare to build the assembly station.

To prepare to build prototypes in FY93, the engineering layouts of alignment equipment were integrated with the mechanical assembly hardware layouts for the precision pick and place machine. These engineering drawings defined the commercial hardware and custom parts needed for the assembly station. Based on the layouts we were able to order the commercial parts for assembly station.

3.4.2 Stability Measurements and Stability Monitoring After the prototypes are constructed in FY93, their assembly precision will be verified and their mechanical stability will be measured. We plan to use a coordinate measuring machine to verify the assembly precision and TV holography to measure stability.

TV holography, the cornerstone of our stability verification technique, is an interferometric method to measure real time shape changes of non optical parts. It is the only technique we know of, with micron precision and large field of view, that will measure prototype subassembly stability in an operating environment. Future experiments using a precision directed X-Ray source to illuminate detectors with powered up electronics, will be used for the final stability studies, but X-Rays are not a suitable tool for early prototypes tests using engineering grade silicon. Early prototype measurements are necessary and important to verify mechanical design, and this is the niche where we believe TV holographic interferometry will be most useful. This year we built a TV holography system to prepare for prototype stability testing in FY93. A typical TV holography schematic is shown in Fig. 5. We first benchmarked the technique on simple aluminum cantilevered beams, and then, we tested silicon ladder assemblies with different loading arrangements. Some of the loading conditions simulated possible types of assembly setup errors. Examples of our TV holography data, are shown in Figures 6, 7 and 8. The test part was made by bonding two silicon ladders to two graphite epoxy blocks near each end to form an H beam, and then, mounting one end to a precision (x,y,z) stage and the other end to an optical rotation stage. With this arrangement we could translate or rotate one end of the beam like assembly relative to the other and measure the shape change induced by the relative motion. Some typical results are shown in Figure 6. The first interferogram and wire frame show how the shape changes when the assembly is bent by 3 μm. The shape change has the characteristic "S" shape we calculate with a finite element code, although we have not yet tried for a detailed match between theory and experiment. The next two interferograms and wire frames show the shape change induced by rotating one end of the silicon ladder assembly relative to the other, and the last interferogram and wire frame show the result of hand heating the block for approximately 10 seconds. These interferograms are snap shots of a continuous stream of data. Beam bending and twisting is monitored quasi-continuously on the TV monitor at the camera framing rate. The

information can also be stored on a VCR for later analysis. It is important to understand that the technique measures shape changes from a base shape. Large shape changes can be measured by bootstrapping to a new base shape when the fringes become too dense, and then, adding the results at the end of the experiment. We plan to use this technique to monitor the shape changes that occur in prototype subassemblies as they are cooled from room temperature to 0 °C. We will also monitor the stability of the subassembly shape in a typical near equilibrium environment. Figures 7 and 8 show the dynamic shape of the same silicon ladder assembly when it is driven with a small audio speaker. When the speaker frequency is near an assembly resonant frequency, the assembly vibrates in a shape that is characteristic for the assembly with the imposed boundary conditions. For this structure the resonant frequencies are not sharp, and the mode shapes are shown only for frequencies close to the peak of each resonant response. The voltage numbers give an indication of the strength of the resonance. Although TV holography has been available for several years, this is the first time we have used it in our laboratory. We still have much to learn about using this tool for STS prototype stability measurements, but it appears that TV holography will be a useful tool.

APPENDIX D

3.2 Design and Development Activities

3.2.1 Enclosure and Supports

The STS' enclosure and support system performs two important functions. This shell assembly provides containment of the evaporated butane coolant, making it a vapor space, as well as serving as the primary conduit for transferring the STS space frame's mechanical loads to the outer tracker space frame. The outer structure and the associated kinematic mounts prevent extraneous loads from being directly imposed on the delicate silicon shell structures, while also maintaining precision alignment. The outer shell structure, hence, is fundamental in maintaining the dimensional stability of the STS.

An ultralightweight G/C-E sandwich-wall vessel is the baseline construction approach chosen for the outer shell and its end cover plates. A 0.5 mm-thin beryllium shell will provide an inner cladding, or liner, for the vessel. This combination, whose wall structures are described in Table 3.2-1, will provide a stiff, low-mass structure for STS support. Because the butane cooling system operates at one atmosphere of pressure, during normal operation the shell structures will not experience a pressure differential. Filling and emptying the butane system will also be accomplished without imposing a significant pressure differential. Consequently, gravitational loads associated with the various structural components principally dictate the stiffness requirements for the outer shell.

In contrast to the outer shell, the end cover structural design is dictated by the 0.2 atm. maximum design pressure differential conservatively chosen for this system. Access to the internal cable connections at both detector ends is provided by the removable end covers. Provisions for *in situ* access for minor reworking of these cables and the flange seal may be desired. It is therefore highly desirable that the outermost shell and flange combination be sufficiently stiff to sustain the STS' entire support reactions without the covers in place. This prospect motivated the choice of a sandwich shell wall construction bearing a truss core with a 45° included angle providing considerable longitudinal stiffness to minimize gravity sag along the shell axis. In addition, the truss core will be circumferentially reinforced, as depicted in Fig. 4-41, in the vicinity of the shell flange to minimize radial deflection when the covers are absent. The flange, which will be fabricated as a G/C-E honeycomb structure, provides most of the circumferential stiffness necessary for the STS mounting surface.

Table 3.2-1 Enclosure description

Component	Material	Size	Remarks
Outer shell	P75/954-3	5.6 m long x 1.2 m diam.	Truss core sandwich wall 3, 300-μm-thick G/C-E lamina
Inner shell	Beryllium	5.6 m long x 10 cm diam.	0.5 mm wall w/reinforcing ribs
End covers	P75/954-3	1.2 m diam. x 2.54 cm wall	Double truss core composite 5, 300-μm-thick G/C-E lamina

To facilitate STS assembly and detector maintenance, the outer enclosure will be composed of multiple sections. Flanges, at discrete intervals, significantly enhance radial stiffness, as previously described. It is desirable that the internal space frame mechanical loads be transmitted to the outer shell at these reinforcements points. Because the outer enclosure is an integral part of the STS support system, the structural design of this particular element is quite critical. Before proceeding with construction of a shell prototype, an analysis of the various shell design parameters was undertaken and is described in the following section.

STS Enclosure FEA Model

The loading conditions for the nominal, or baseline, solution were held constant for the static and dynamic analyses. These conditions were

- 0.2 atm. of external pressure on the enclosure's cylindrical sections and end caps.

- The weight of approximately 100 kg of distributed space frame mass attached to the enclosure, and

- The weight of the enclosure.

A buckling analysis was performed in which only the midsection of the enclosure shell was considered because of that region's susceptibility to buckling.

The boundary conditions for the model were designed to simulate a kinematic mounting scheme composed of three bars that are tangent to the enclosures surface. Three curved beam elements intersecting the enclosure's perimeter with 120° of separation provide an idealized, self-centering STS enclosure mount. In practice, the three beams would terminate at the outer tracker space frame to which they would transfer the STS' and its enclosure's loads. A detailed study of the STS mounting philosophy and approach will be discussed later in this document.

The materials properties of the enclosure's sandwich facings and core as well as the physical dimensions of these elements were varied parametrically using the FEA. The results of these investigations will now be discussed.

STS Enclosure Static FEA Results

The enclosure static analysis demonstrated the maximum resultant displacement for the nominal case, excluding the domed ends, occurred in the cylindrical portion. The maximum stress concentration occurred around the cylinder and end flanges, where the end caps attach. Not surprisingly, the most effective means found for reducing these deflections was to increase the sandwich facing thickness and elastic modulus, as depicted in Figures 3.2.1-1 and 3.2.1-2. Specifically, the maximum deflection associated with doubling the 0.2 mm, nominal-case, facing thickness was a reduction from 0.22 mm to 0.15 mm and a reduction of Von Mises stress from 32 MPa to 16.6 MPa. Similarly, when doubling the 103 GPa, nominal-case, elastic modulus, the maximum deflection and Von Mises stresses were reduced from the nominal-case values to 0.125 mm and 33.6 MPa, respectively. A graphic comparison of the effect of elastic modulus on the deflection of the enclosure is found in Figure 3.2.1-3. For comparison, the elastic modulus of the G/C-E, nominal-case, material is 103 GPa. As previously discussed, the relationship between the sandwich core shear modulus and its thickness and geometry is well understood (REF. FY91 R&D REPORT HERE). Therefore, a study was performed only on the core shear modulus variation on the enclosure's radial deflection with the core geometry and thickness held constant. The typical decrease in displacement experienced by the shell with an increase in core modulus can be seen in Figure 3.2.1-4.

S. Ney #9

3.2.1-1

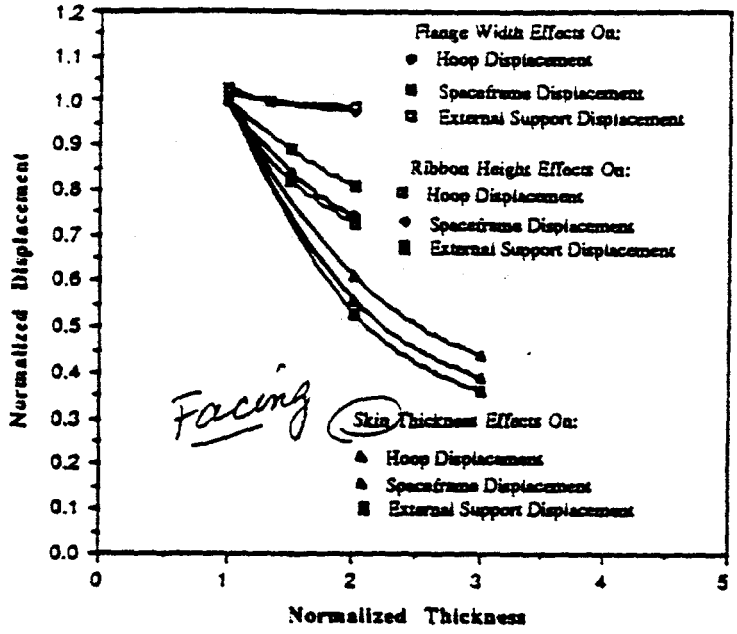

Higher Resolution Req'd

Figure 3.2.1-1. Enclosure normalized displacement expressed as a function of sandwich facing thickness.

S. Ney #10

3.2.1-2

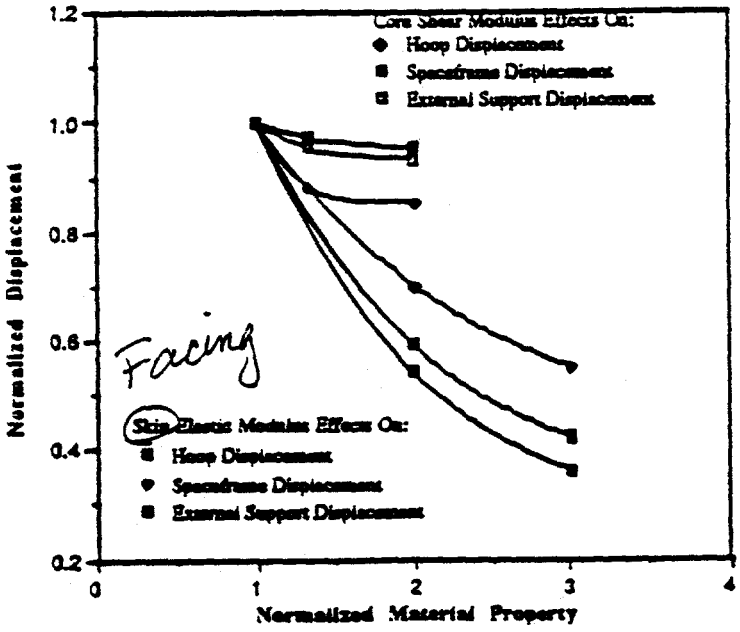

Higher Resolution Req'd

Figure 3.2.1-2. Enclosure normalized displacement expressed as a function of sandwich facing elastic modulus.

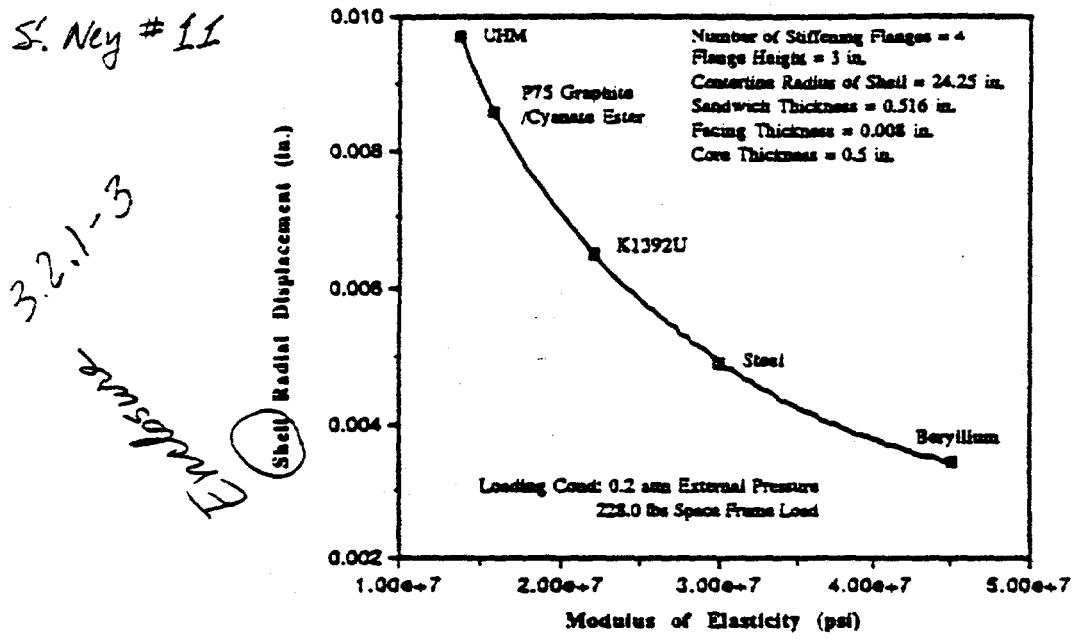

Figure 3.2.1-3. Enclosure radial displacement expressed as a function of sandwich facing elastic modulus.

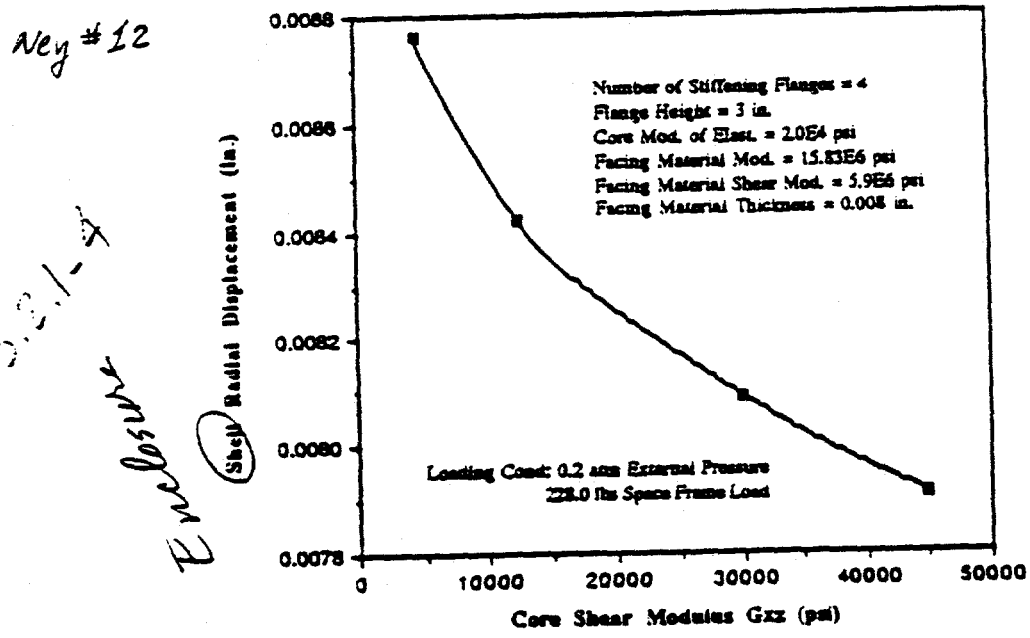

Figure 3.2.1-4. Enclosure radial displacement expressed as a function of sandwich core shear modulus.

STS Enclosure Dynamic FEA Results

The fundamental and second natural frequencies of vibration of the enclosure are ovalization modes, possessing two circumferential lobes, about orthogonal basis axes. This was expected because of the vessel's small length to diameter ratio. Furthermore, the third and fourth modes were characterized by three circumferential lobes about basis axes 120° apart. The frequencies of these vibrations were approximately 84 Hz for modes one and two and approximately 166 Hz for modes three and four of the nominal case. The deformed configurations of these modes are displayed in Figures 3.2.1-5 and 3.2.1-6. Parametric studies of sandwich core thickness and elastic modulus demonstrated that to achieve a fundamental vibrational frequency of 100 Hz, using the nominal-case core elastic modulus, a core thickness of 19 mm would be required. This 100 Hz fundamental frequency will provide ample margin for materials performance uncertainties.

STS Enclosure Buckling FEA Results

The enclosure's central section was analyzed as an unreinforced, nominal-case, vacuum vessel and as a flange-stiffened and facing-thickened vessel. For 0.2 atm. of external differential pressure and nominal-case materials properties, a 0.7 atm. critical buckling pressure was determined. The results of a parametric study of the number and dimensions of intermediate stiffening flanges on vessel buckling performance is shown in Figure 3.2.1-7. Also, the effect of sandwich facing thickness on this pressure is displayed in Figure 3.2.1-8. It is clear from these graphs that a buckling factor of safety of 5, for a differential pressure of 0.2 atm., can be easily achieved by adding one intermediate stiffening flange. This must be compared to achieving almost the same performance by increasing the facing thickness to 0.3 mm. Unlike adding the flange, the increased facing thickness would appreciably improve the deflections and stresses experienced by the vessel as well as distribute the added material more uniformly over the volume.

5 Neg #17

3.2.1-5

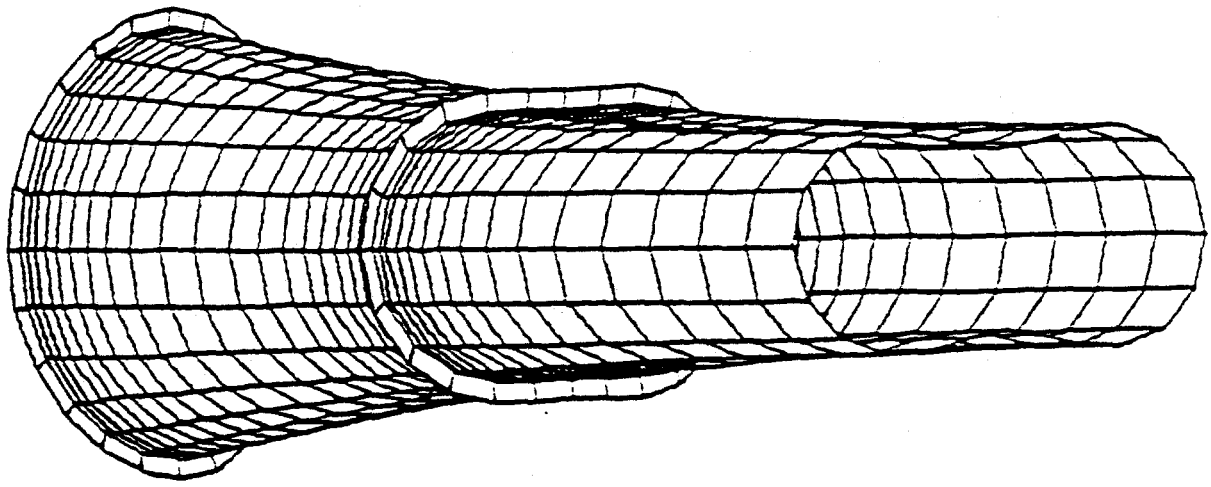

Figure 3.2.1-5. Enclosure fundamental natural frequency of vibration deformed configuration.

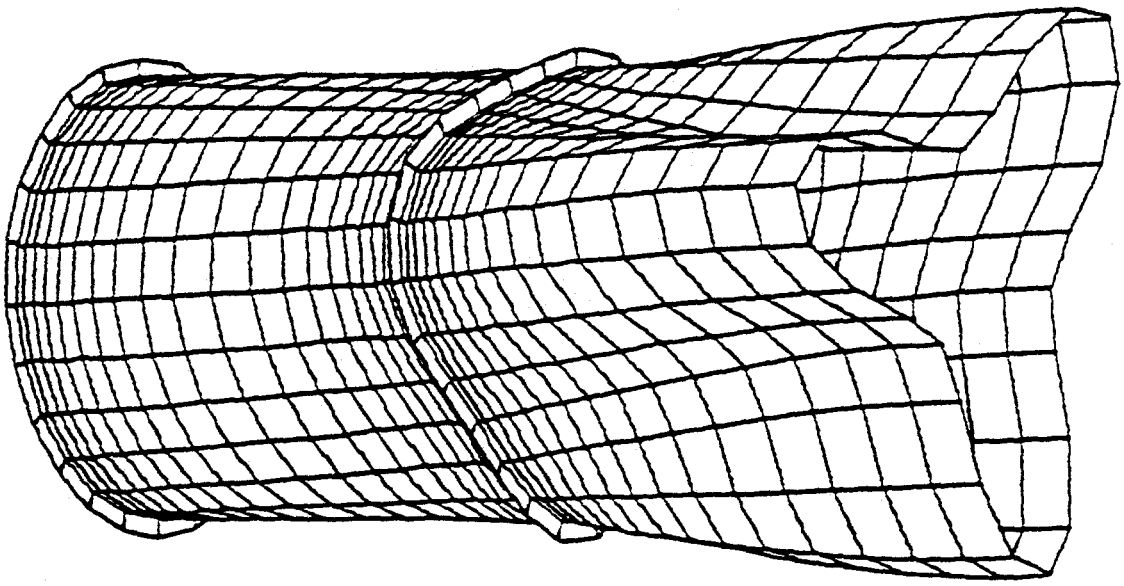

Figure 3.2.1-6. Enclosure third natural frequency of vibration deformed configuration.

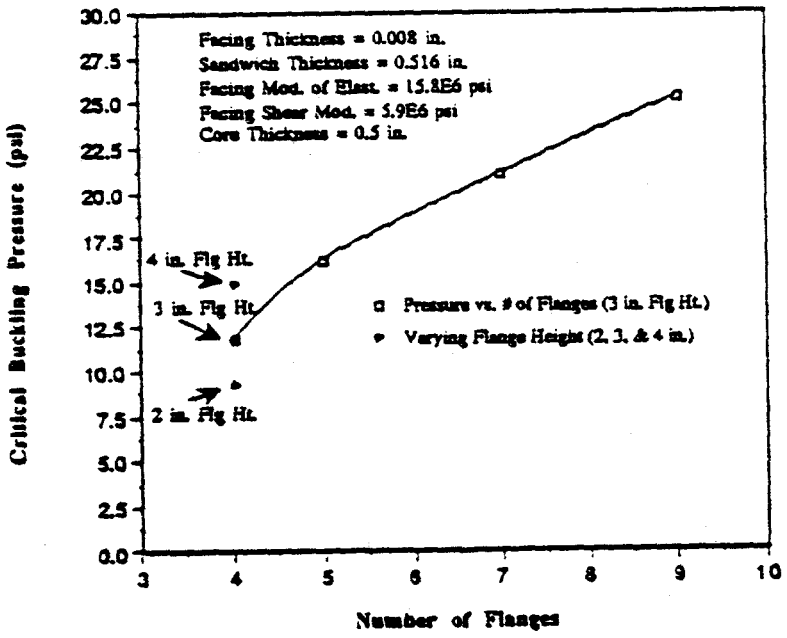

Figure 3.2.1-7. Enclosure buckling performance expressed as a function of number of intermediate stiffening flanges.

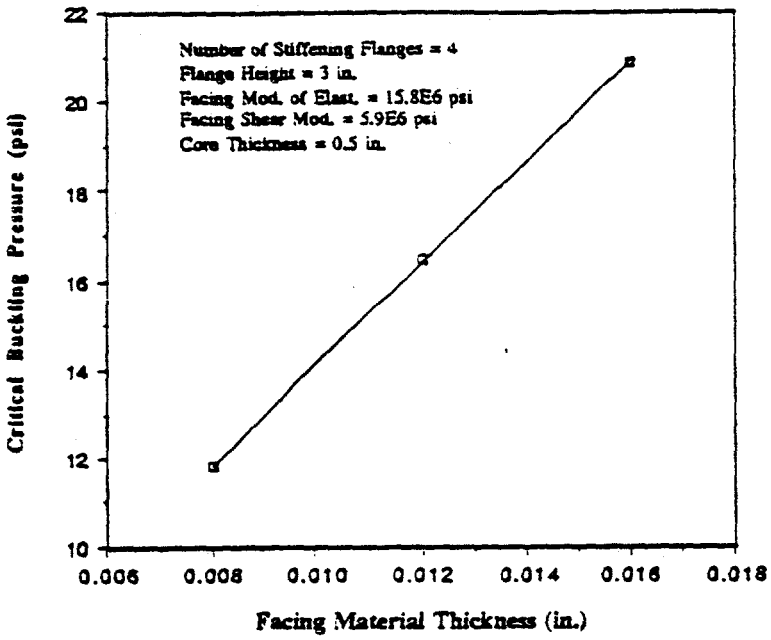

Figure 3.2.1-8. Enclosure buckling performance expressed as a function of sandwich facing thickness.

STS Enclosure FEA Conclusions

These preliminary FEA results clearly indicate several areas for optimization. Generally, the most sensitive parameters for the static, dynamic, and buckling performance of the enclosure shell are the sandwich facing thickness and elastic modulus. The mechanical strength of the design constituents was shown not to be an issue. The decision to increase the thickness and / or the elastic modulus of the nominal case must be considered in the presence of other ramifications on the overall system. An increase in radiation length would result from increasing facing thickness. The fabrication difficulty, availability, and cost of 690 GPa elastic modulus graphite fibers also have a negative influence on this issue.

The unconventional nature of a truss-core sandwich construction mandates prototyping exercises. These will illuminate the enclosure design considerably and can be used to normalize the FEA results obtained thus far. After careful deliberation on the analytical and test results, a new outer enclosure baseline design will be forged.